NONLINEAR OPTICS AND BIO-SENSING WITH SILICON NITRIDE WAVEGUIDES

by

SUBRATA DAS

DISSERTATION

Submitted in partial fulfillment of the requirements
For the degree of Doctor of Philosophy at
The University of Texas at Arlington
December, 2019

Arlington, Texas

Supervising Committee:

Michael Vasilyev, Supervising Professor
Robert Magnusson
Kambiz Alavi
Weidong Zhou
Alice Sun

Acknowledgements

ABSTRACT

Nonlinear Optics and Bio-sensing with Silicon Nitride Waveguides

Subrata Das, Ph.D.

The University of Texas at Arlington, 2019

Supervising Professor: Michael Vasilyev

Silicon Nitride (SiN) is a CMOS compatible optical material that can be used for both linear and nonlinear optics applications. SiN has high refractive index (1.99-2.0) and low two photon absorption (TPA) coefficient. As a result, SiN can be used as a core material to guide and bend light, and the development of compact on-chip SiN optical devices exploiting both linear and nonlinear optical phenomena is very much feasible.

In this thesis work, two independent research projects are presented. The first work presents the design of a hybrid SiN/Polymer slot waveguide for second-harmonic generation (SHG) of a 1550-nm wave at 775 nm. This is a simulation-based work where the waveguide dimensions are numerically optimized to fulfill the conditions required for SHG in a bended structure, i.e. microring. This work presents an optimum slot waveguide design with very high effective nonlinearity, with a critical slot dimension of 200 nm that is very much attainable in a class 100 cleanroom facility like Shimadzu Institute- Nanotechnology Research Center, University of Texas at Arlington and shows prospect of developing waveguide and micro-resonator based nonlinear photonic integrated circuits.

In the second project, a microring resonator has been designed, fabricated and characterized for biosensing applications. The fabrication steps are discussed thoroughly so that it can be replicated in future research endeavors. This fabricated optical biosensor has been designed to work in aqueous environment, so that the presence of particular biomaterial, in this case Neuropeptide Y (NPY), can be easily detected and quantified according to sample concentration at μg/ml level. The experimental investigations confirm that the detection limit of this microring resonator in a single assay system is 1 μg/ml with a sensitivity of 0.1 nm/(μg/ml). This sensitivity can be amplified by a factor of 3 by using sandwiched assay system, and NPY concentration at 0.25 μg/ml level was successfully detected.

Contents

List of Figures

List of Tables

Chapter 1

Introduction

Over the last two decades Photonics has crossed its infancy and grew up as a matured technology field. From research labs to industry, photonics announces its viable candidacy against 'Electronics'. From the year 2000, scientists working in Optics and Photonics has won Nobel Prizes for five terms for their groundbreaking works on Optical Coherence, Optical Fiber, Blue LED, Optical Tweezer and Optoelectronics. Yet several years will definitely be required for photonics to gain the supremacy over electronics. One of the main reasons behind this delay is the absence of a single material like 'Silicon', which is abundant as 'sand' yet works as a 'pillar stone' for the electronic industry. As a result, scientists and researchers thought, why not building the photonic integrated circuit (PIC) on the shoulder of silicon? They envisioned for Silicon Photonics [1]. This has the advantage of CMOS compatibility which paved the way to integrate with electronic circuitry [2.] As a result, silicon on insulator (SOI) has emerged as the basis for PIC where a thin layer of silicon is deposited on top of a silicon oxide (SiO_2) layer [3]. The high index contrast between SiO_2 and Si made it possible to develop waveguide-based linear optic devices that can guide, bend the optical signal [4]. But to become the ubiquitous technology, several solutions are still required to be demonstrated on industry scale and at commercial level.

Future optical sensing, communications, and signal-processing systems will need to be compact, environmentally-robust, and energy-efficient. These requirements raise the need for on-

chip integration of nonlinear-optical devices (e.g., parametric amplifiers, wavelength converters, and second-harmonic generators) with sources, detectors, and other linear optics components used in such systems. While promising $\chi^{(3)}$-based platforms are emerging continuously [5–7], $\chi^{(3)}$ devices suffer from parasitic Raman and higher-order mixing processes degrading their noise properties (e.g., limiting the noise figure of a "noiseless" phase-sensitive amplifier to just over 1 dB [8, 9]). $\chi^{(2)}$ interaction is free from such noises and can therefore be attractive for future low-noise-classical and quantum information processing applications [10]. However, the focus of $\chi^{(2)}$ integrated photonics has largely remained on Periodically Poled Lithium Niobate (PPLN) and Periodically Poled Potassium Titanyl Phosphate (PPKTP) waveguides, whose inherent losses and low index contrast limit the scale of integration.

Silicon is also well known for its nonlinearity. But due to centrosymmetric crystal structure $\chi^{(2)}$ based nonlinear effects are absence in its true form. So, to demonstrate $\chi^{(2)}$ processes, i.e. electro-optic effect, in Si we need to break the symmetry either by strain or by introducing interface with other material [2]. For better $\chi^{(2)}$ integration potential, a hybrid approach combining silicon waveguides with nonlinear polymer cladding was introduced [11, 12]. However, nonlinear-optic applications of silicon-based devices are limited by the two-photon absorption (TPA).

1.1 Silicon Nitride as an Optical Material:

Apart from continuing research in silicon photonics, other materials with similar prospect are also under incubation process. Among them, Silicon Nitride (Si_3N_4 or SiN for short) drew the most attention due to its familiarity in CMOS technology. SiN has been an indispensable part for decades in Micro-Electro-Mechanical Systems (MEMS) fabrication processes where it is mostly used as a passivation layer and as insulation material [13]. It has high refractive index (1.9–2.0) and low absorption in both telecom / near-IR and visible wavelength ranges, which makes it

possible to be used in compact photonic circuits with tight bending radii [14–17]. SiN has nonlinear characteristics like Si and it also shows centrosymmetry or inversion symmetry. But the reason that brought more attention into SiN based nonlinear optics research lies in its high-power handling capability owing to negligible TPA, while exhibiting a relatively high nonlinear refractive index n_2 suitable for $\chi^{(3)}$ applications [18–23].

1.1.1 SiN - platform for on-chip sensing:
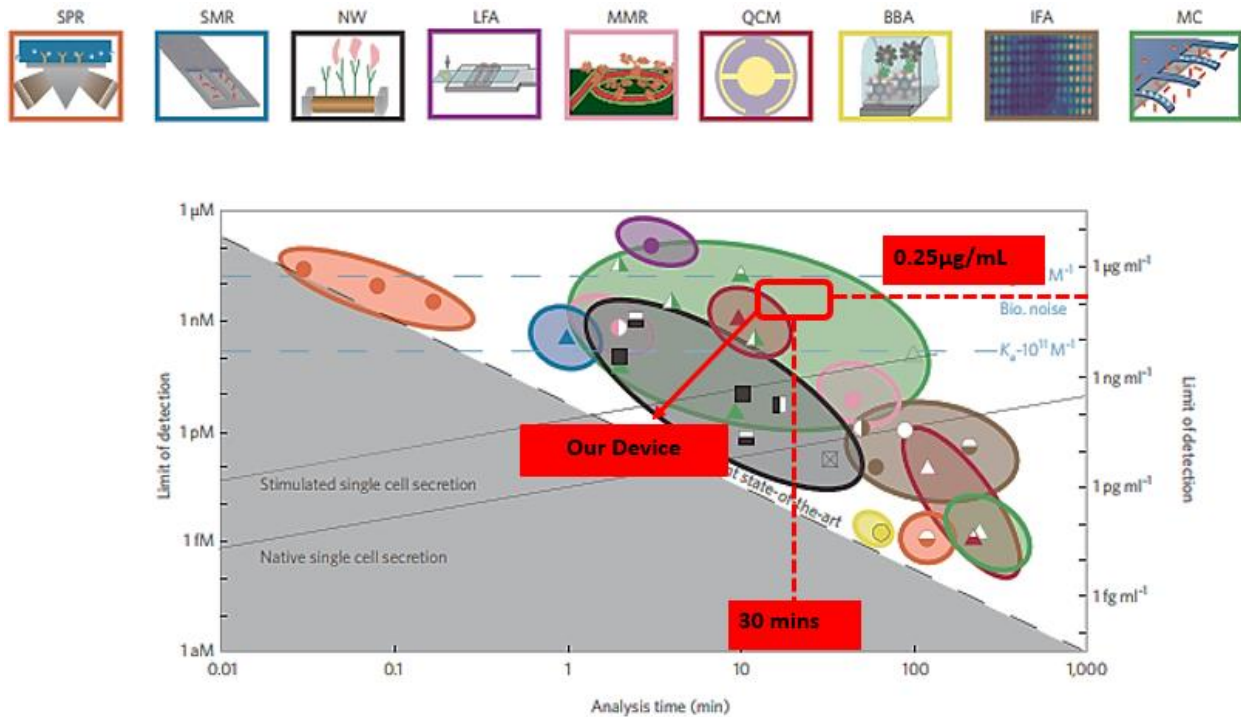
Fig. 1-1. Comparison of different biosensing methods (from [27]).

Here, SPR= Surface plasmon resonance; SMR= Suspended microchannel resonator; NW= Nanowire; LFA= Lateral Flow Assay; MRR= Microring resonator; QCM= Quartz Crystal microbalance; BBA= biobarcode amplification assay; IFA= immunofluorescent assay; MC= microcantilever.

The light guiding facility owing to high refractive index and the CMOS compatibility can be extended to make SiN as a platform for on-chip sensing applications [24-25]. The need for real-time monitoring of certain physiochemical activities in human body has created demand for low-power wearable sensors and emerging technologies of sensors on-a-chip [26]. These

technologies are becoming more and more efficient and integrated these days. Based on sensing principle and the underlying device structure there are several biosensors available. Figure 1-1 gives a comparative illustration between these biosensors with respect to their detection limit in both moles and gm/ml scale versus respective time of analysis. Here the black dashed line represents the state-of-the-art detection limit with respect to the time required for analysis.

One of the very attractive on-chip sensing platforms is based on evanescent field sensing /refractive index sensing. In this case, the sensor surface is first functionalized with immobilized bio-receptors to capture the target analyte by affinity binding [28]. These sensors may utilize microdisk, microring, or racetrack as the resonating device [29], in which a tail of the optical mode spreads into the cladding region that slightly changes its refractive index when analyte attaches to it. It is an indirect sensing approach where the change in transmission spectra owing to change in effective index is being related to the concentration of the analytes. In Fig. 1-1 the pink ellipse represents the performance results from microring resonator-based biosensors. We see that the limit of detection lies in between 0.6 nM (50 ng/ml) to 6.5 pM (100 pg/ml) with an analysis time in the range of 2 mins to 45 mins.

In this present work, a microring-resonator-based label-free ex-vivo optical sensor has been fabricated and evaluated to investigate the detection of Neuropeptide Y. Using sandwiched assay, we detected NPY concentration down to 0.25 µg/ml with a 30 minutes analysis time. Thus, we can ascertain that the performance of our device is well comparable with other micoring-resonator-based biosensors as shown by the red box imposed on the Fig. 1-1.

1.1.2 Second Harmonic Generation in SiN Waveguide:

SiN can also be used for nonlinear optics applications. But due to centro-symmetry $\chi^{(2)}$ in Eq. (1-1) vanishes for SiN. Thus, nonlinear processes like Optical Parametric Oscillation (OPO),

Difference Frequency Generation (DFG), Second harmonic Generation (SHG), Sum Frequency Generation (SFG)- are not available with SiN crystal.

$$\mathbf{P}(t) = \epsilon_0 \left[\chi^{(1)} E(t) + \chi^{(2)} E^2(t) + \chi^{(3)} E^3(t) + \ldots \ldots \ldots \right] \tag{1-1}$$

Equation (1-1) shows the relationship between induced polarization, P(t) in a material in response to the application of a highly intense electric field [30]. Here, ϵ_0 is the free space permittivity, $\chi^{(1)}$ is the linear susceptibility and $\chi^{(2)}$, $\chi^{(3)}$ are the second and third order nonlinear optical susceptibility.

Applications of $\chi^{(2)}$ processes span from optical communication to molecular spectroscopy. Many biomolecules have characteristic footprint in certain wavelength region where a light source may not be readily available [21]. As a result, wavelength conversion through $\chi^{(2)}$ process is a plausible solution in that case. Figure 1-2 shows the schematic of SHG, where an input signal at ω_1 frequency with high enough power generates an output signal at ω_2 frequency through nonlinear interaction within the $\chi^{(2)}$ material.
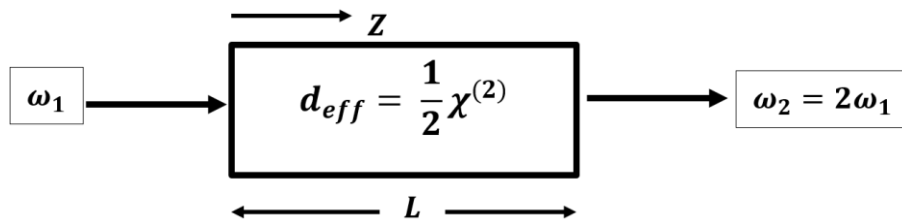
Fig. 1-2. Schematic of Second Harmonic Generation [31].

Weak second order nonlinear processes can still be generated using SiN waveguide if the symmetry is broken, i.e. at the surface [31, 32] or after electric-field poling [33]. Effective $\chi^{(2)}$ nonlinearity in SiN microrings has also been achieved in four-wave-mixing-based coherent photon conversion scheme [34].

As a part of the thesis work, a hybrid SiN waveguide with nonlinear polymer material has been designed and evaluated for SHG at 1550 nm. The necessary conditions for generating second harmonic are fulfilled by optimized tuning of the waveguide dimensions.

1.2 Motivation:

a) Silicon Nitride (SiN) is good optical material for both linear and nonlinear optics applications.

b) SiN as an attractive alternative to Si with added benefits of high-power handling capability due to negligible TPA

c) To explore $\chi^{(2)}$ - based integrated devices by utilizing hybrid SiN with polymer approach

d) Application of SiN microring structure in sensing purposes.

1.3 Objectives:

i) Investigate Hybrid Silicon-Nitride/Polymer Waveguides for Second- Harmonic Generation (SHG).

ii) Development of Silicon Nitride microring resonator and demonstrate its application as a refractive index sensor.

1.4 Outline of the Thesis:

In this thesis work two independent projects has been accomplished which are related to the two objectives stated in previous section. The first project aims to show the nonlinear optics aspect of SiN by designing a slot waveguide capable of demonstrating second harmonic generation (SHG) at 1550 nm. The second project shows the CMOS compatibility of SiN by fabricating a microring resonator and shows it applicability in linear optics by utilizing that microring resonator as a biosensing device.

The individual discussions on these two project-works are presented as part I (Chapter 2) and part II (Chapter 3) in this dissertation. The first project is mainly about exploring the possibility

of generating second harmonic in SiN-polymer hybrid waveguide at 1550 nm. So, part I contains the theoretical background on SHG conditions and simulation parameters required for designing and modelling of the waveguide. It also presents the results obtained from the investigation of single channel waveguide and slot waveguide. Finally, it discussed the effect of bending in such a waveguide structure. The results from this project has already been published in two conference papers [35,36] and in one journal paper [37]. As a result, part I contains the text from those publications.

Part II is related to the second project on the investigation of Neuropeptide Y detection by a SiN microring resonator. So, this part of the dissertation discusses the sensing principle, fabrication processes and characterization techniques followed in the experiment. Also, the sample preparation steps and working procedures are also highlighted in the later part of this section. Some results from this work has already been published as two conference papers [26,38] and some results are yet to be published. So, this part contains texts from these publications.

Finally, in chapter 4 the thesis work has been summarized under the light of the objectives stated in chapter 1.

Chapter 2

Investigation of Hybrid Silicon-Nitride/Polymer Waveguides for Second-Harmonic Generation

2.1 Introduction:

SiN is a potential material for nonlinear optics applications. In this chapter, we describe design of a hybrid SiN waveguide with nonlinear polymer cladding suitable for making efficient $\chi^{(2)}$-based devices. As an example, we considered the generation of second-harmonic in this present work. Apart from Second-harmonic generation (SHG) there are several other nonlinear optics applications like sum frequency generation (SFG), difference frequency generation (DFG) etc all of which are based on $\chi^{(2)}$ phenomenon [30]. Due to the central symmetry, $\chi^{(2)}$ effects in SiN-based non-hybrid structures only manifest themselves either at the surface by breaking inversion symmetry [31, 32] or after electric-field poling [33] and are very weak.

The SiN waveguide dimensions are numerically optimized to simultaneously achieve the phase matching and maximize the nonlinear overlap integral between the interacting waves. We discussed preliminary results of this study at two conferences [35,36]. The present chapter is our complete report on full optimization of the waveguide geometry over a wide practical parameter range and it has been published as a journal article [37]. Section 2.2 introduces the two important conditions for SHG- phase matching condition and the nonlinear overlap integral. We start by studying a single channel waveguide in Section 2.3, achieving the modal phase matching in both TM and TE cases. However, the nonlinear overlap in the polymer cladding region is found to be

extremely small, making the single channel waveguide very inefficient for nonlinear-optical applications. In Section 2.4, we turn to investigation of a slot-based waveguide and find that it meets the goals of both phase matching and maximizing nonlinear overlap integral. In Section 2.4.3 we also show that the slot-based waveguide is robust with respect to bending with reasonable radii down to ~150 μm, which permits its use in microresonators. Section 2.5 summarizes this work.

2.2 Theoretical Background:

Device, that exploit second-order nonlinear effects, must meet two conditions:

1) satisfy phase matching of the interacting waves, which is necessary for accumulation of the nonlinear effects over the entire propagation distance, and

2) have a large effective nonlinearity, which is determined both by the $\chi^{(2)}$ tensor elements of the nonlinear material and by the overlap integral of the nonlinear material and the interacting modes [35,39].

The wave vector mismatch between the participating waves is totally zero in a case of perfectly phase matched condition,

$$\Delta k = k_1 - k_2 = 0 \tag{2.1}$$

At this situation the generated wave remains at a fixed phase relation with the input wave and can extract the total energy from it efficiently. Phase matching can be attained by birefringence, quasi phase matching (QPM) or by Modal Phase Matching (MPM) [40]. Si_3N_4 is not a birefringent material so angle tuning mechanism [30] for phase matching cannot be carried out. On the other hand, special fabrication process is required to ensure the periodic inversion of crystalline axis required for QPM. In this present work, modal phase matching (MPM) [39-41] between 0th-order mode of the near-infrared (1550-nm) fundamental wave and 2nd-order mode of the SHG wave (775 nm) has been employed. This technique is similar to the one previously used in SiN-surface-

based SHG [32], and it builds upon our work on multimode parametric amplification [41-43] and mode-selective wavelength conversion [39, 43-46]. Propagating the fundamental and SHG waves in two different waveguide modes presents an opportunity to overcome the material and waveguide dispersions and achieve perfect phase matching by making the effective refractive indices of these modes equal:

$$n_{\text{eff}}^{m,1550} = n_{\text{eff}}^{n,775} \tag{2.2}$$

where m and n are the mode orders of the fundamental (wavelength $\lambda_{1550} = 1550$ nm) and SHG (wavelength $\lambda_{775} = 775$ nm) waves, respectively. Under normal dispersion conditions, typical for waveguides fabricated from relatively thin SiN films (a few hundred nm thick), the phase matching requires $n > m$.

Once the phase-matching condition is satisfied, one needs to maximize the effective nonlinearity. For a given choice of the material with nonlinear constant d_{eff}, this means maximizing the nonlinear overlap integral Φ of the two interacting modes and the nonlinear material

$$\Phi = \frac{1}{A_{\text{eff}}} = \frac{\left|\int_{-\infty}^{\infty}\int_{-\infty}^{\infty}\theta(x,y)\Psi_{m,1550}^2(x,y)\Psi_{n,775}^*(x,y)dxdy\right|^2}{\left[\int_{-\infty}^{\infty}\int_{-\infty}^{\infty}|\Psi_{m,1550}(x,y)|^2dxdy\right]^2\int_{-\infty}^{\infty}\int_{-\infty}^{\infty}|\Psi_{n,775}(x,y)|^2dxdy} \tag{2.3}$$

which also equals the inverse effective area A_{eff} of the SHG interaction. In Eq. (2.2), $\Psi_{m,1550}$ and $\Psi_{n,775}$ are the electric-field profiles of the mth-order mode at λ_{1550} and n^{th}-order mode at λ_{775}, respectively. $\theta(x,y)$ shows the transverse distribution of the nonlinear material: it equals 1 within the nonlinear polymer and 0 outside of it. Since $\theta(x,y)$ is typically an even function of x ($x = 0$ at waveguide's vertical line of symmetry), $\Psi_{n,775}$ must also be an even function of x; otherwise, Φ becomes zero. The lowest orders satisfying both this and $n > m$ conditions are $m = 0$, $n = 2$, on which we focus from now on. The normalized small-signal SHG conversion efficiency η is related to fundamental power P_{1550}, SHG power P_{775}, and waveguide length L by

$$\eta = P_{775}/(P_{1550}L)^2 = 8\pi^2 d_{\text{eff}}^2\Phi/[(n_{\text{eff}}^{m,1550})^3\lambda_{1550}^2\varepsilon_0 c] \tag{2.4}$$

2.3 Brief Description of the Simulation Process:
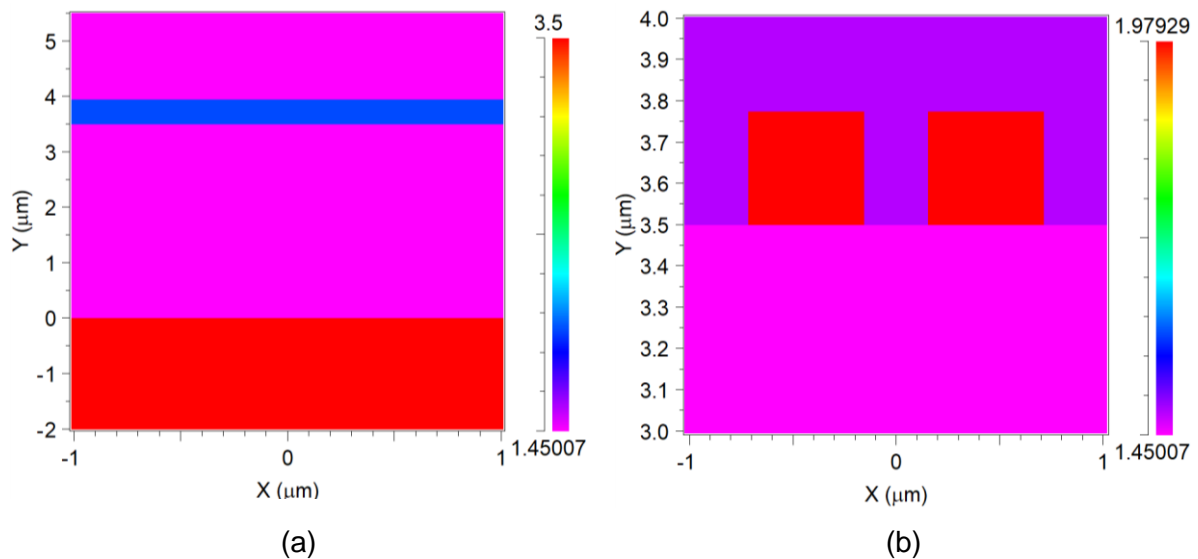
Fig. 2-1. Contour map of transverse index profile for (a) slab waveguide- index varies only in Y direction, (b) slot waveguide- index varies in both X and Y direction. Color bar on the side represents the index value.

The waveguide structure, considered in this work, is modeled by RSoft / Synopsys BeamPROP software, which uses finite-difference beam propagation method (FD-BPM) [47]. This method solves paraxial approximation of Helmholtz equation with certain assumptions to represent light propagation in a complex waveguide structure. The successful design of the structure depends on several parameter-optimizations. Some of the design issues are pointed out here so that interested reader may reproduce the structure for their own interest.

- Global Setting Window: Here the default settings of the simulations are created
  - Simulation Tool- BeamPROP, Dimensions- 3D, 3D Structure Type- Multilayer
- Layer Table Editor: It is required to define individual layers' height and refractive index.
  - Single layer table is sufficient for structures where there is no variation of index horizontally, i.e. infinite length slab waveguide Fig. 2-1 (a)
  - For index variation in horizontal direction, i.e. slot waveguide in Fig. 2-1(b), more than one CAD structure is required and individual index table for each of the CAD has to be built.
- All the design parameters are defined in the Symbol Table Editor.

- 'Display Material Profile' button shows contour map of transverse index profile as in Fig. 2-1.
- Properties of each segment can be checked by clicking right button on the CAD structure.
  - Additional component properties like "Simulated Bend" are found under the button "More".
- Launch Parameter button in the main window brings all parameters related to the input launch field. In this present case a "MultiMode" type launch field has been used.
- Finally, the mode profile is calculated by using the "Mode Calculation Parameters" button.
  - There the polarization of input beam can also be set either at TE or TM.
  - Mode calculation method, boundary condition, numerical scheme, Pade Order, BPM vector mode, grid size- all these essential parameters are also available in this window.

2.4 Investigation of a Single Channel Waveguide:
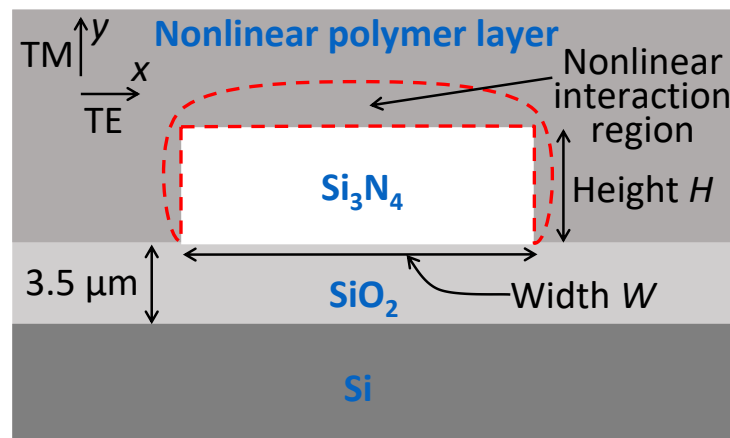
Fig. 2-2. Schematic of the single channel waveguide. Nonlinear $\chi^{(2)}$ interaction occurs within the upper-cladding region with red dashed-line border.

We first consider a simple single channel waveguide with upper cladding made of a nonlinear polymer, as shown in Fig. 2-2. Here the Si$_3$N$_4$ core guides light and the polymer material takes care of the nonlinearity. The waveguide's lower cladding is a 2.5-µm-thick layer of thermally-grown silicon dioxide (SiO$_2$), which provides sufficient mode isolation from the Si substrate. We find from Sellmeier equation [48] the refractive indices of 1.998 (1.979) for stoichiometric SiN, i.e., Si$_3$N$_4$, core and 1.454 (1.450) for SiO$_2$ lower cladding at 775 nm (1550 nm) wavelength and

assume index of 1.46 for a generic nonlinear polymer. In effective-index and mode-profile calculations, the polymer nonlinearity is neglected. We start with a typical SiN waveguide with dimensions 1 μm × 0.32 μm ($W \times H$), which does not require growing thick SiN films. It supports single 1550-nm and three 775-nm spatial modes. The mode profiles at 1550 nm and 775 nm are shown in Fig. 2-3, where TE corresponds to the horizontally-polarized (non-zero E_x) and TM corresponds to the vertically-polarized (non-zero E_y) electric field. Next, we vary the width W and height H of the waveguide to achieve modal phase-matching separately for TE- and TM-polarized cases [49], with the results shown in Fig. 2-4. As can be seen in Fig. 2-4, phase-matching for TM polarization can be obtained by varying either width or height of the SiN core, whereas phase-matching for TE polarization can only be obtained by varying the waveguide width.
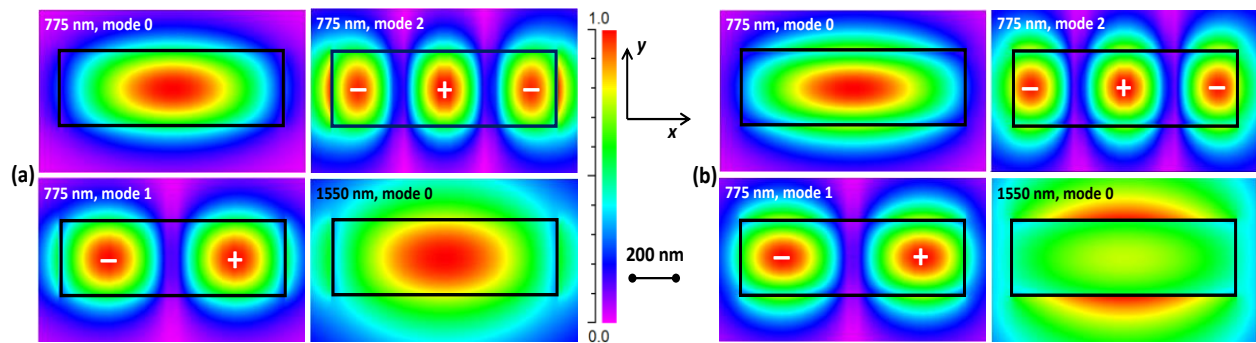
Fig. 2-3. 775-nm and 1550-nm mode profiles for (a) TE-polarized ($|E_x|$ is shown) and (b) TM-polarized ($|E_y|$ is shown) cases in a 1 μm × 0.32 μm single channel waveguide. Black rectangles show the border of SiN core. "±" symbols indicate relative signs of different lobes.
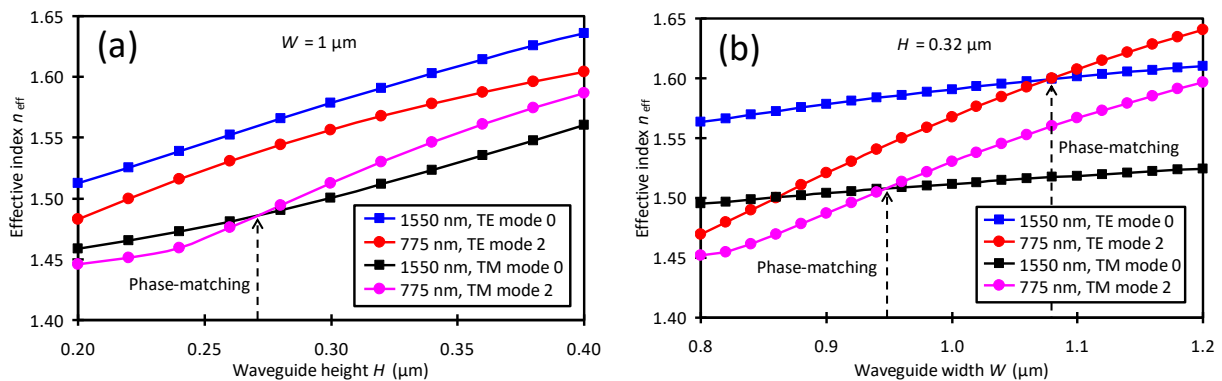
Fig. 2-4. Obtaining modal phase-matching condition of Eq. (1) by varying single channel waveguide's (a) height H or (b) width W.

Table 2-I. Single channel waveguide dimensions resulting in phase matching, as well as the corresponding effective areas.

Waveguide dimensions $W \times H$ (μm)	Polarization	Effective area A_{eff} (μm^2)
1.08×0.320	TE	234
1.00×0.275	TM	203
0.95×0.320	TM	210

The values of width W and height H corresponding to the phase-matched condition, as well as the resulting values of the effective area A_{eff} of SHG interaction are summarized in Table 2-I for both TE- and TM-polarized cases. The results in Table 2-I indicate that in a single-core waveguide structure the effective area A_{eff} of SHG interaction is too large (~200 μm^2) to yield an efficient nonlinear process. The reason for this is the fact that all three lobes of the 2nd-order SHG mode overlap with the fundamental wave in the nonlinear polymer cladding region. Compared to the central lobe, the outer lobes provide opposite-sign contribution to the overlap integral Φ of Eq. (2.3), largely canceling the central-lobe's contribution and greatly reducing Φ (and, hence, increasing A_{eff}). To maximize the overlap integral, it would be highly desirable to reduce the contribution of the outer lobes to Φ by reducing either their overlap with the fundamental wave or their overlap with the nonlinear material, while keeping the contribution of the central lobe intact. As we will see in the next Section, this can be achieved in a double-core waveguide structure (slot waveguide).

2.5 Investigation of a Slot Waveguide:

Slot waveguide consists of two channel cores of high refractive index, separated by a narrow gap (slot). The low-index slot has a width that is usually less than the decay length of the field extending from the cores [50]. One of the advantages of the slot waveguide is the wide range of dispersion engineering realizable with it [51, 52]. Perhaps, its even more important advantage is the possibility of a significant enhancement of the electric-field due to discontinuity at the slot-

core interface [53, 54]. When the slot is filled by a nonlinear polymer material, this field enhancement can be used for nonlinear-optical applications: silicon-organic hybrid double-slot waveguides [12] and hetero-slot waveguides consisting of SiN and aluminum nitride [55] were proposed for $\chi^{(2)}$ nonlinear processes in mid-infrared range. In this Section, we study a simple single-slot waveguide design and show its suitability for SHG by achieving phase matching and maximizing nonlinear overlap integral through optimization of waveguide geometry. We also describe the robustness of this design with respect to bending with reasonable radii down to ~150 μm, which permits its use in microresonators.

2.5.1 Design and Optimization:

We model and optimize the hybrid slot waveguide structure of Fig. 2-5, where upper cladding made of a nonlinear polymer also extends into the slot between the two SiN channel waveguides. We concentrate on the TE mode (horizontally-polarized electric field), because its electric field is significantly enhanced in the slot region, compared to the TM mode.
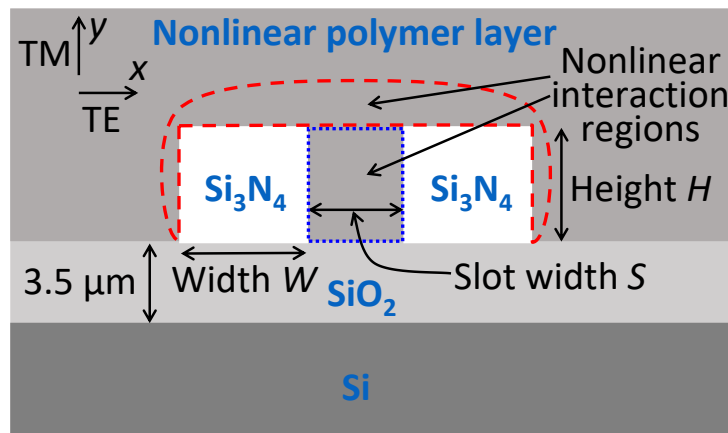
Fig. 2-5. Schematic of the slot waveguide with two SiN cores. Nonlinear $\chi^{(2)}$ interaction occurs within the slot region with blue dotted-line border and within the upper-cladding region with red dashed-line border.

Figure 2-6 shows the TE spatial modes supported by the slot waveguide with width $W = 589$ nm, height $H = 450$ nm, and slot width $S = 200$ nm: 2 at 1550 nm and 4 at 775 nm. These modes can be related to symmetric and anti-symmetric superpositions of the similar modes of the two distant

channel waveguides. When the two channels are moved close to each other, their coupling makes these superpositions non-degenerate. In the symmetric (even-order) modes the fields from the two channels add in phase in the slot region. We will consider interaction between $m = 0$ mode at 1550 nm and $n = 2$ mode at 775 nm, for both of which the field in the nonlinear slot is strongly enhanced. Note that the negative-sign outer lobes of the 2nd-order 775-nm mode do not extend into the field-enhanced slot region and overlap only with weak tails of the 0th-order 1550-nm mode, which limits their negative impact on Φ. We optimize two cases having same linear (effective indices, mode structure), but different nonlinear (overlap Φ) properties: a) nonlinear polymer confined only to the slot region, whereas the upper cladding is made of a strictly linear polymer; b) nonlinear polymer extending to both slot and upper cladding regions.
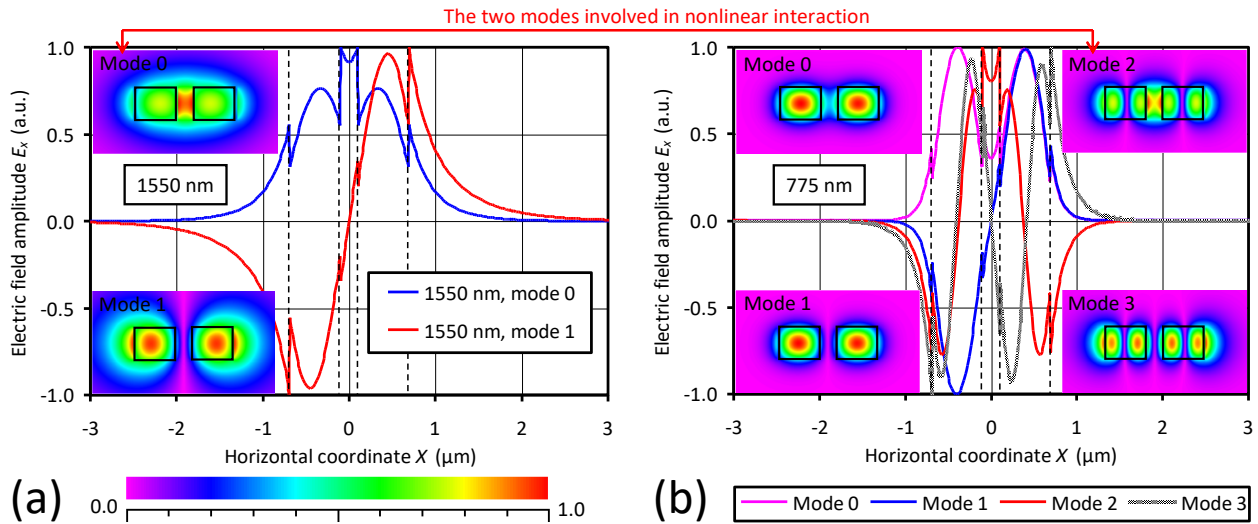
Fig. 2-6. TE mode profiles for (a) 1550 nm and (b) 775 nm beams. Black boxes (dashed lines) in the inserts (line graphs) show the borders of the SiN cores.

We start optimization of the slot waveguide geometry from the parameters of the optimum single channel waveguide for the TE case (1.08 μm $W \times$ 0.32 μm H), divide its width by two, and insert a 0.1–0.5-μm gap between the two halves (limited by practical fabrication constraints on the lower side [56] and by decreasing nonlinear overlap on the higher side). The height of the waveguide corresponds to the thickness of SiN layer, growth of which is limited by the high tensile stress

[57]. To optimize, we independently vary the waveguide height H and slot width S, choose each channel width W to satisfy the phase-matching condition for given H and S, and then finally calculate the overlap integral of Eq. (2.3) for each combination. Figure 2-7a shows the resulting effective interaction area A_{eff} as a function of waveguide height H for two values of slot width, $S = 200$ nm and $S = 310$ nm. In all cases, the optimum height is near 450 nm. Next, we vary the slot width S while keeping the height H at 450 nm (the width W is always adjusted to obtain the phase matching) and plot the resulting values of A_{eff} in Fig. 2-7b. We see that the effective area monotonically increases with slot width, initially very slowly (in 100...150-nm region) and then linearly (after ~175 nm). Even though the smallest slot widths offer marginally smaller A_{eff} values, etching of narrow slots with high-aspect-ratio (100 nm wide × 450 nm deep) is very challenging.
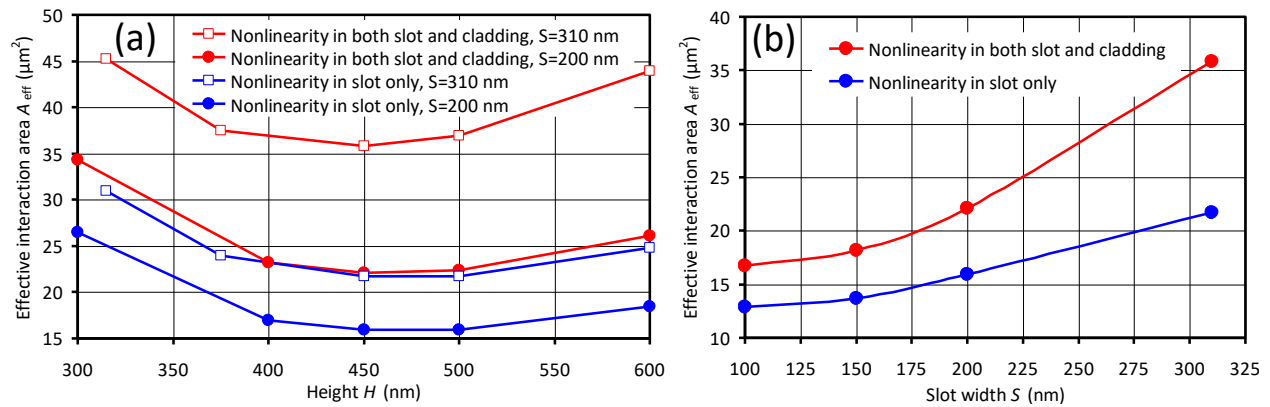
Fig. 2-7. Dependence of the effective interaction area A_{eff} (a) on waveguide height H for fixed slot widths $S = 200$ nm and $S = 310$ nm and (b) on slot width S for optimum waveguide height $H = 450$ nm. At every point, the channel width W is optimized to satisfy the phase-matching condition.

We choose $S = 200$ nm as the smallest practical slot width, and, according to Fig. 2-7b, it yields A_{eff} within 20% from its global minimum value. For the optimum combination of height $H = 450$ nm and slot width $S = 200$ nm, the phase matching is achieved at channel width $W = 589$ nm. Figure 2-8a shows effective indices n_{eff} of various 775-nm and 1550-nm modes versus slot width S at optimum values of $H = 450$ nm and $W = 589$ nm. The curves for 0th-order fundamental mode and 2nd-order SHG mode almost overlap in a wide region around design value of $S = 200$ nm,

indicating nearly non-critical phase-matching that is robust to fabrication errors. Figure 2-8b shows the wavelength dependence of the effective index for the optimum slot waveguide (W = 589 nm, H = 450 nm, S= 200 nm) in the vicinity of the phase-matching wavelength. Detuning from the design wavelength changes the effective index by $\Delta n_{eff} \approx 0.015$ per 100 nm of wavelength change. This can be used to estimate the shift of the phase-matched wavelength owing to fabrication errors.
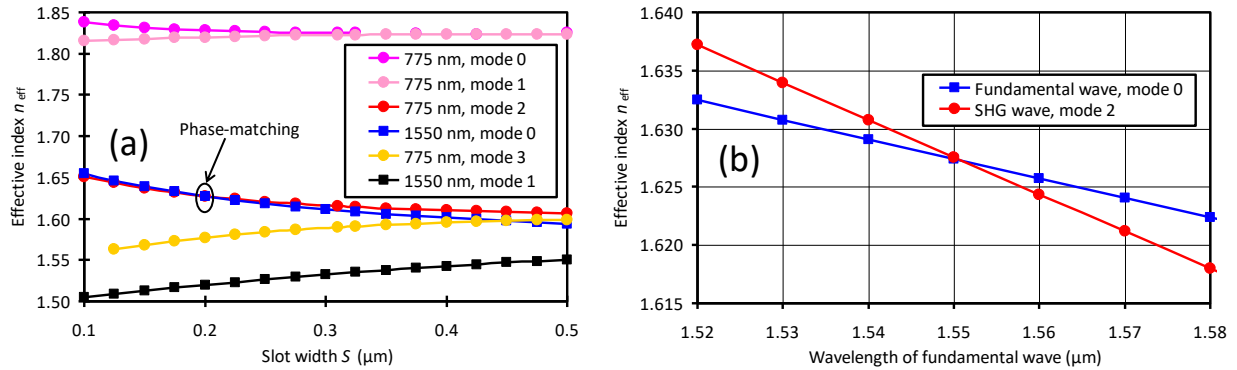
Fig. 2-8. (a) Slot-width dependence of the effective indices of all supported TE modes of the waveguide with optimum height H = 450 nm and width W = 589 nm. (b) Effective refractive index of the optimum slot waveguide (S = 200 nm) as a function of wavelength.

2.5.2 Results and Discussion:

The results of the optimization are summarized in Table 2-2. For polymer that fills both the slot and the upper cladding, we have obtained the minimum effective area A_{eff} = 22.1 µm^2. The effective area can be further reduced by using polymer only in the slot region and filling the rest of the upper cladding by a linear polymer (or by SiO$_2$). In that case, the overlap-reducing contribution of the two negative outer lobes of the 2nd-order SHG mode (red curve in Fig. 2-6b) completely vanishes [there is no nonlinear polymer, i.e., $\theta(x,y) = 0$, in the region of the outer lobes], and the resulting effective area is reduced to A_{eff} = 15.9 µm^2. For comparison, we also show the optimized values of the effective area for TM-polarized case. Unlike TE wave, TM wave does not benefit from the field enhancement in the slot, and its effective area is comparable (more precisely, somewhat larger) than that in the single channel waveguide case. The optimized TE

case compares favorably to typical values of $A_{\text{eff}} \approx 25 \ \mu\text{m}^2$ and $A_{\text{eff}} \approx 60 \ \mu\text{m}^2$ for SHG in single- and two-mode [45,46] PPLN waveguides, respectively. The nonlinear polymers have high $d_{\text{eff}} \sim$ 100–500 pm/V [11, 58]. Even for a conservative value of $d_{\text{eff}} \sim 20$ pm/V, Eq. (2.4) yields conversion efficiency $\eta = 730\%$ / W / cm^2 for TE case with $A_{\text{eff}} = 15.9 \ \mu\text{m}^2$, which is an order of magnitude more efficient than single-mode PPLN ($\eta \approx 70\%$ / W / cm^2). With low SiN loss (< 0.5 dB/cm) [6], cm-scale waveguides are feasible.

Table 2-2. Optimized slot waveguide dimensions resulting in both phase-matching and minimized effective areas.

Optimized waveguide dimensions $W \times H \times S$ (µm)	Polarization	Effective interaction area A_{eff} (µm^2)	
		Nonlinearity in both slot and cladding	Nonlinearity in slot region only
$0.589 \times 0.45 \times 0.20$	TE	22.1	15.9
$0.5 \times 0.3 \times 0.33$	TM	404	308

2.5.3 Effect of Bending:

To explore the use of the hybrid SiN / polymer slot waveguide in microrings, we analyze the effect of bending on the optimum slot waveguide ($W = 589$ nm, $H = 450$ nm, $S = 200$ nm) by employing the simulated bend method of RSoft BeamPROP [47]. This method maps a bent waveguide onto a straight waveguide by a coordinate transformation. The waveguide length is taken as a quarter arc with a radius $R = c / (2\pi \ n_{\text{eff}} \ \Delta\nu) = 146.7 \ \mu\text{m}$, corresponding to a microring with free spectral range $\Delta\nu = 200$ GHz and phase-matched effective index $n_{\text{eff}} = 1.6274$. We consider TE case only and find that bending slightly shifts the phase-matching wavelength. This shift can be compensated by either a small change in the waveguide dimensions (e.g., ~3 nm change in channel width W) or by a slight (< 10 nm) shift of the slot position towards the center of curvature [59], as shown in Fig. 2-9a. In Figure 2-9a the slot position is varied with respect to the center of the structure in a range from –100 nm to 100 nm, which corresponds to the movement towards outside and inside of the bend, respectively. Such shift of the slot does not significantly

impact the effective area A_{eff} of Eq. (2.3), as shown in Fig. 2-9b. 10-nm shift of the slot reduces A_{eff} by about 2.1% when the polymer is only in the slot region and by about 1.7% when the polymer is in both slot and upper cladding regions. These results prove the robustness of the hybrid SiN / polymer waveguide to bending.
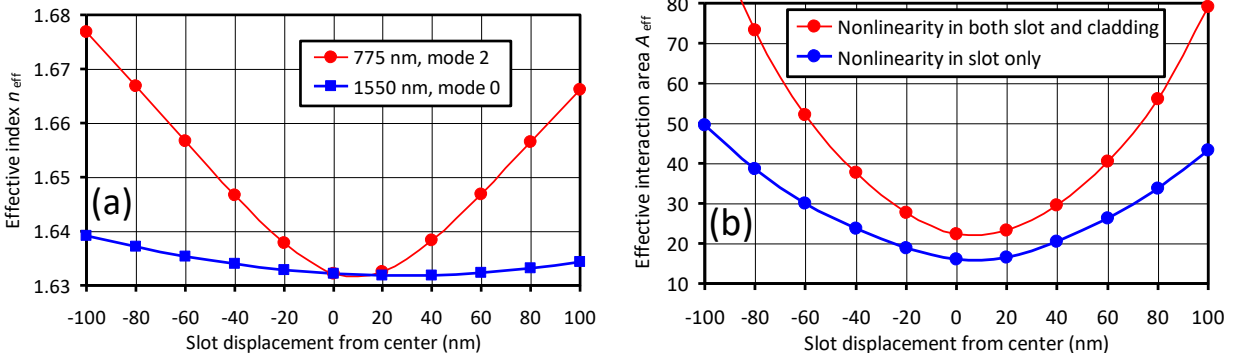
Fig. 2-9. Effects of the slot position in a bent waveguide (a) on the effective indices n_{eff} of the interacting modes and (b) on the effective interaction area A_{eff}.

2.6 Summary:

We have discussed the design and optimization of a SiN waveguide with polymer cladding layer to generate second harmonic of a 1550-nm wave. We have shown that a single channel waveguide can be optimized to achieve the phase matching condition between 0th-order fundamental and 2nd-order second-harmonic modes, but the effective nonlinearity in this case is very low due to a poor nonlinear overlap integral. In contrast, an optimized slot waveguide with nonlinear polymer filling either the slot or both the slot and upper cladding has an order-of-magnitude higher nonlinear overlap integral. We have shown that both phase-matching condition and the nonlinear overlap integral are robust with respect to fabrication errors and to waveguide bending with radii as small as ~150 μm, which is promising for the development of waveguide- and microresonator-based nonlinear photonic integrated circuits. The conversion between a fundamental Gaussian beam and a higher-order waveguide mode can be easily done by a phase plate or a spatial light modulator [45,46].

Chapter 3

Investigation of Neuropeptide Y Detection by a Silicon-Nitride Microring Resonator

3.1 Introduction:

In this chapter, investigation of Neuropeptide Y (NPY) detection by a Si_3N_4 microring resonator is presented. NPY is commonly associated with human stress. It is a 36-amino-acid-long neuropeptide involved in cardiovascular physiology, feeding, anxiety, depression and epilepsy [60]. The underlying physical principle of the detection method is the Evanescent Field sensing technique [28]. The microring resonator is thus required to be designed in such a fashion that a significant amount of the mode extends into the cladding area and demonstrate its sensitivity to cladding's refractive index change. Thus, the performance of this sensor solely depends on the well optimized designing of the waveguide structure and its fabrication steps.

In this present work, the waveguide structure is modelled and designed by using BeamPROP, a Beam Propagation Method (BPM) based commercially available design tool from RSoft/ Synopsys [47]. Figure 3-1 shows the schematic of the waveguide structure. The dimensions of the waveguide are optimized so that it supports only the fundamental mode at 1550 nm of wavelength.
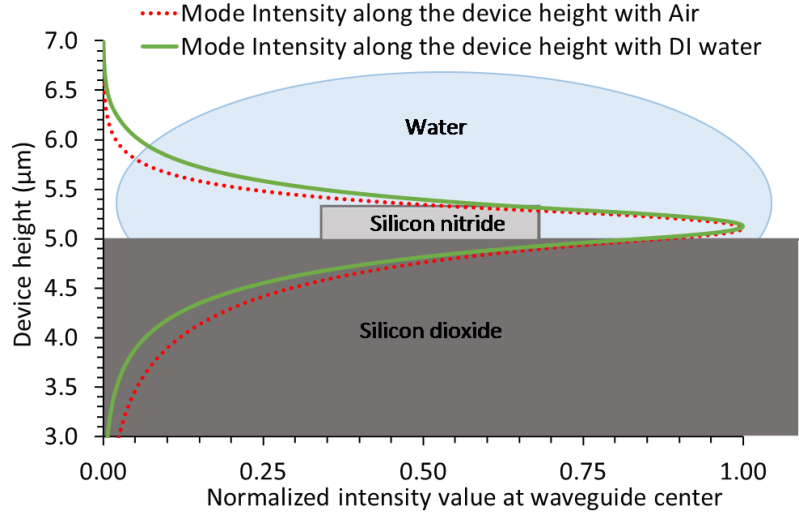
Fig. 3-1. Device schematic with normalized intensity profile along device height (X-Z cross section).

The red and green curves depict the mode profiles for air cladding and DI water cladding, respectively. The extension of the mode tail into the upper cladding layer depends on the index contrast between the cladding and the core- the lesser the index difference the higher the extension of mode tail into the cladding area. As a result, in Fig. 1 we can observe that green trace (DI water) expanded more into the cladding area compared to the red one (air) and it is because DI water offers less index contrast compared to air with respect to the same core material- Si_3N_3. This variation in mode profile is the resultant of the effective index variation of the waveguide. As a result, the resonance wavelength of the microring will change as $\Delta\lambda/\lambda = \Delta n_{\text{eff}}/n_{\text{eff}}$ [29]. In case of a sensor, the amount of shift in resonance wavelength can be related to the concentration of any substance in a solution.

Before going into the detail of NPY detection the fabrication steps of the microring resonator and its sensitivity analysis as a sensor are required to be discussed. Using standard CMOS technology facilities, Si_3N_4 microring resonator with thick (> 1 µm) SiO_2 upper cladding and Q factor ~10^5 was previously fabricated in our research group [61]. In this present work, only a very thin top coat of SiO_2 (thickness ~20 nm) has been deposited, so that the mode can

evanescently interact with the analyte. The Q factor obtained with the present device is between 5000 and 8000 due to the thin cladding layer, which makes it more sensitive to surface roughness and environmental perturbations, increasing the losses.

3.2 Fabrication Process of Microring Resonator

The microring resonator has been fabricated on silicon wafer utilizing several CMOS processes steps. Silicon wafers with thermally grown oxide layer of thickness 5 μm was purchased. This thick oxide layer works as the bottom cladding layer, which is essentially thick enough to isolate the mode from the substrate. These wafers are then cleaned and prepared for CMOS processes required to develop the target device.

3.2.1 Low Pressure Chemical Vapor Deposition (LPCVD):

A stoichiometric Silicon Nitride layer of 280 nm is deposited over the oxide (SiO_2) layer by LPCVD process. The optimized thickness is chosen based on two considerations:

1) Maximize core thickness to accommodate about 70% -80% of the beam width of the fundamental mode.

2) Minimize SiN core thickness to avoid high tensile stress [57].

The cleanroom at Shimadzu Nanotechnology Research Center, University of Texas at Arlington (UTA) has both the PECVD and LPCVD facilities to develop Silicon Nitride layer. LPCVD is preferred over PECVD to avoid probable stress in nitride layer and to obtain better uniformity. The low pressure onto the

Fig. 3-2. LPCVD System for Si_3N_4 layer deposition located at UTA Cleanroom [62].

reactant molecules helps them to be densified on the surface with very low defects. The Tystar

TYTAN 3600 equipment for LPCVD, as shown in Fig. 3-2, can create film thickness in the range

of 0.1- 2 µm. Due to low deposition rate (3-3.5 nm/min) film uniformity is also high [62]. The

process parameters are stated in the Table: 3-1.

Table 3-1. Process parameters for SiN LPCVD

Gas Mixture Ratio	Dichlorosilane (DCS): Ammonia (NH$_3$) → 1:3
Furnace Pressure	250 mT
Temperature	770° C.

The gases in the furnace participated in the following chemical reaction to create Si$_3$N$_4$ layer onto

wafer surface:

$$4 \text{ NH}_3 + 3 \text{ SiH}_2\text{Cl}_2 \rightarrow 6 \text{ HCl} + \text{Si}_3\text{N}_4 + 6 \text{ H}_2 \tag{3.1}$$
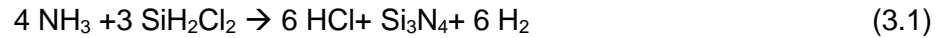
The deposition has been carried out in two steps at the rate of 25 Å/min and the wafers were

cooled down to room temperature between the two steps to avoid stress at high temperature. The

uniformity of the deposited SiN layer is verified by using reflectometer and the deviation in the

uniformity is found to be less than 3%. The wafers are then diced into 12 mm x 12 mm pieces and

cleaned for next processing step.

3.2.2 E Beam Lithography:

The E Beam lithography process consists of three sub steps:

a) **Spin Coating of E beam resist:** The end target of the E Beam lithography is to create

ridge waveguide of SiN as shown in the Fig. 3-3. To achieve this, negative E Beam resist

(ma-N 2405) is used in present case [63]. The sample is first cleaned in acetone for 5 mins

with ultrasonic agitation followed by a 2min long ultrasonic agitation in methanol. Finally,

the samples went through a 10 min long ultrasonic agitation in deionized (DI) water and

dried up by N_2 gas purge system. The cleaned samples are then baked for 20 mins on hot plate at a temperature of 150º C. As a result, the moisture evaporates from the sample surfaces. The samples are then spin coated with negative resist ma- N2405 at 3000 rpm for 30 sec and subsequently kept on hot plate at 95º C for 2 mins. According to the datasheet [63] a 0.5 µm thick resist is deposited and it is confirmed under profilometer by creating a scratch at a corner.

280 nm thick Si_3N_4

Si wafer with 5 µm thick thermal SiO_2

Spin coated E beam negative resist MAN 2405
280 nm thick Si_3N_4

Si wafer with 5 µm thick thermal SiO_2

280 nm thick Si_3N_4

Si wafer with 5 µm thick thermal SiO_2
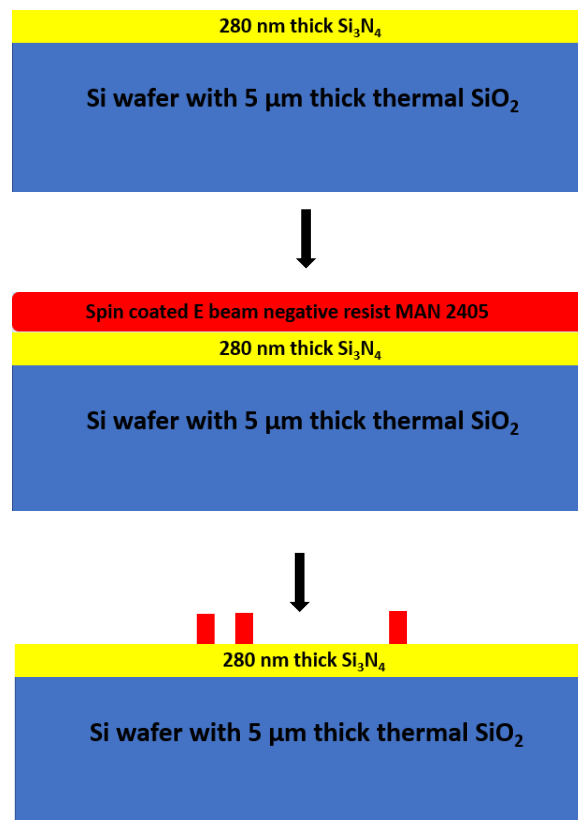
Fig. 3-3. Schematic of the E Beam lithography process

b) **CAD design in NPGS (Nanometer Pattern Generation System):** As we are going to pattern in E Beam lithography we do not need any mask rather we need a CAD file containing the design pattern which we want to be replicated on to the samples. NPGS is a simple yet well capable CAD design tool. In its simplest form the final device consists of

a ring resonator and a bus waveguide that couples light in and out from it. Figure 3-4 shows the schematic of the structure. First a design area of 12 mm X 12 mm has been considered. The length, L of the bus waveguide, which is the longest dimension in the design, is set to be 4 mm. It is better to get a longer bus waveguide that makes it easier to manually cleave the sample at the final stage using tweezer, but with a price to lower the magnification scale of the writing to fit the total pattern within the field of view. After creating the pattern file, the maximum allowable magnification can be obtained by using the MaxMag feature of NPGS which is a library function that calculate the maximum microscope magnification allowed to fit the pattern within the writing field for an optimized working distance value [64]. The schematic shown in Fig. 3-4 is replicated 8-10 times with a variable Gap, g within a range from 100-500 nm. This variation of gap is done to check the light coupling efficiency from the bus waveguide to the ring. The position of the ring is also moved to right and left from the center. The width of both the bus waveguide and the ring is set to 1 µm and the ring radius is 150 µm.
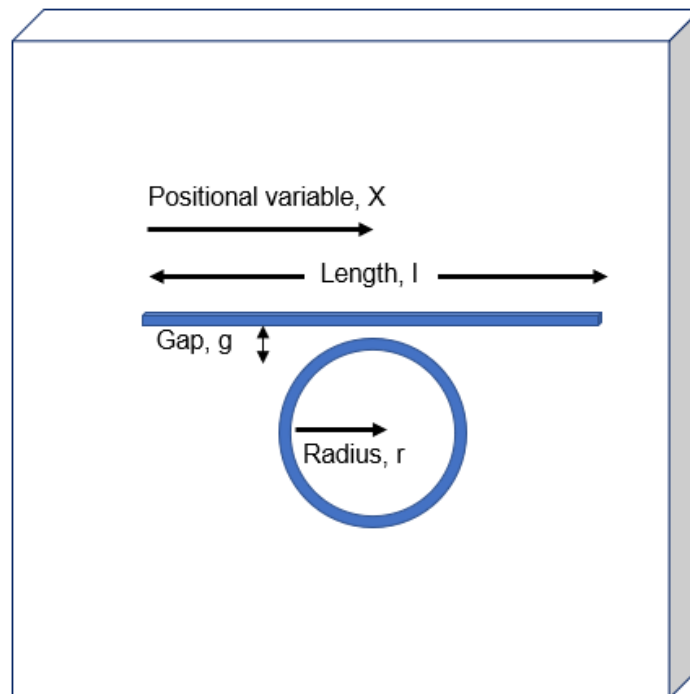
Fig. 3-4. Schematic of NPGS CAD design

c) E Beam Writing: Obtaining a highly focused and precious beam is the root of success with E Beam writing. First, we create a marker on the wafer surface by scratching at a corner keeping in mind that the central area of the wafer should not be exposed. This marker helps to focus on the surface plane at high magnification ~ 200kX. The wafer is then loaded into the vacuum chamber and the marker is brought under the crosswire to adjust the focus at different magnification level, i.e. 300x, 1kx, 20kx etc. As per the manual [65], the system works best at a working distance of around 6.1 mm. At all the magnification levels other focusing parameters- focus wobble, stigmatism should be checked as well. The X-Y coordinate value of the four corners should be taken carefully which will ultimately help to position the beam at correct position during writing. The beam current at the 'Faraday Cup' is also required to be recorded and a value around 35-40 pA is good to get nice features. Table :2 shows all the parameter value used during the E Beam writing. One individual waveguide and ring take around 30 mins to write. The total pattern may take several hours depending on its size. After that the wafer is unloaded from the chamber and brought to cleanroom for development. According to the CAD design only the waveguide and the ring were exposed to the electron beam. As a result, the unexposed resist washed away when we keep the wafer in developer solution Ma-D 525 for 60 seconds. The beaker containing the developer solution slowly agitated every 5 seconds. After 1 minute the wafer is checked under optical microscope to see whether there are still any resist remaining on the wafer specially in the gap between the ring and straight waveguide as shown in Fig. 3-5.

Table 3-2. Process parameter for E Beam Lithography

Parameter	Value
Acceleration Voltage (EHT)	25 KV (maximum is 30 kV)
Beam Current	35 pA- 40 pA
Working Distance	6.1 mm- 6.9 mm

Aperture Number (size)	3 (10 μm)
Writing Magnification	90X- 100X
Faraday Cup Current	35 pA- 40 pA
Exposure Dose*	250-280 μCcm^{-2}

*Check the e beam resist datasheet [63] for the suggested dose.
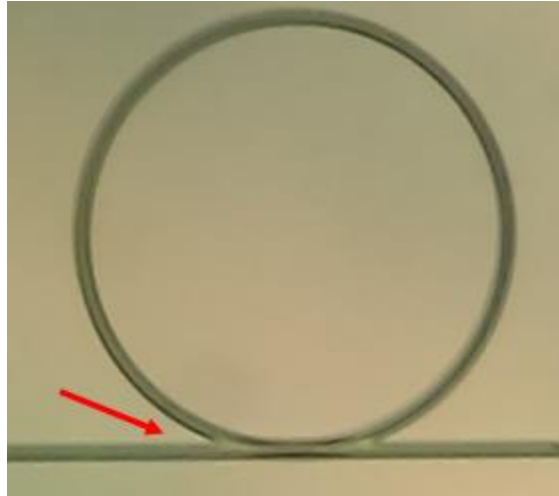
Fig. 3-5. Optical microscope image of the microring resonator after resist development

Sometimes due to proximity effect the resist in the gap area may also be exposed and may remain on the wafer even after developing. In this case agitation in the ultrasonic bath for 5 sec would be helpful. But this should be done carefully as the ultrasonic agitation may also detach the exposed resist that create the pattern. The wafer is then baked on hot plate for 5 mins at 145°C.

3.2.3 Deep Reactive Ion Etching (DRIE):

To etch out the Si$_3$N$_4$ a recipe has been developed for the TRION DRIE system. This tool works on the principle that a high-power RF signal (13.56 MHz), creates plasma by ionizing the etchant gas, in this case it is CHF$_3$ [66,67]. This unstable reactant then etches away Si$_3$N$_4$ by subsequent chemical process shown below:

$$e^- + CHF_3 \rightarrow CHF_2^+ + F + 2\,e^- \tag{3.2}$$

$$Si_3N_4 + 12\,F \rightarrow 3\,SiF_4 + 2\,N_2 \tag{3.3}$$

The etch rate of the nitride layer depends on the fluorocarbon produced as byproduct in the chemical process. This fluorocarbon creates a thin polymer layer on Si_3N_4 and on the chamber wall and thus decreases the etch rate. To get rid of this fluorocarbon layer small amount of O_2 is also introduced into the reaction chamber. This O_2 oxidizes the fluorocarbon and creates CO or CO_2 which evaporate easily. The overall effect is the increase in nitride etch rate. This O_2 also creates volatile oxides of nitrogen that also play positive role in Si_3N_4 etching through active surface reactions. [68,69].
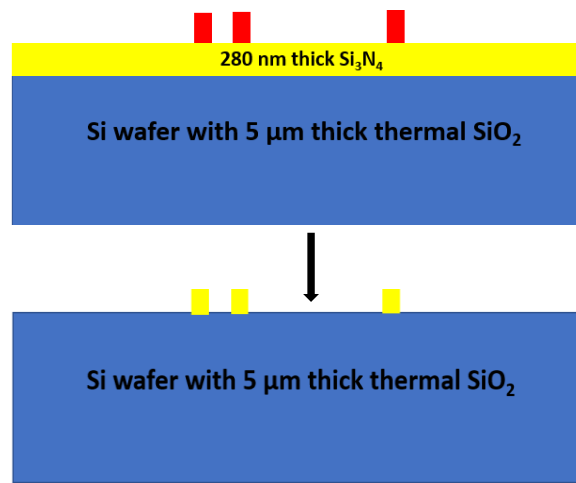
Fig. 3-6. DRIE etch process

The optimized recipe for this etching process is stated in Table:3-3.

Table 3-3. Process parameter for DRIE process of Si_3N_4 layer

Parameter	Step 1	Step 2
Chamber pressure (mT)	16	150
RIE Power- lower electrode (W)	13	0
ICP Power- Upper electrode (W)	2340	0
He Press	3	0
He (sccm)	10	70

O$_2$ (sccm)	2	0
CHF$_3$ (sccm)	21	0

To find out the etch rate of Si$_3$N$_4$, the recipe was run for one minute and the thickness of the remaining nitride layer was measured using reflectometer. Essentially the etch under this recipe was found as 300 Å/min. The set parameters in the DRIE system fluctuates from time to time. So, it is always advisable to run with test wafer first to verify the etch rate.

3.2.4 Thermal Annealing:

The next step in the fabrication process is thermal annealing. This process is quite simple yet highly important. The samples went under DRIE process are cleaned properly with acetone, methanol and rinsed in DI water. The samples are then dried up on hot plate at 150^0 C for 10 mins. This annealing step is required to break the dangling N-H bonds in nitride layer [70] otherwise these bonds have absorption peak in the 1550 nm wavelength range of interest. As a result, the samples are kept under N$_2$ environment in Minibrute Diffusion Furnace for several hours at very high temperature [71]. Both the temperature and the time was optimized after several characterization of several samples. As a result, it was quite tedious to check each and every waveguide performance under illumination at 1550 nm. Finally, we obtain very good IR light coupling by annealing at 1140°C for seven hours. The other way to avoid this long process is to avoid NH$_3$ at the very beginning of LPCVD Si$_3$N$_4$ deposition and to use SiH$_4$ and N$_2$ instead [20]. But the present available LPCVD system at our cleanroom facility supports only the gas mixture of DCS and ammonia (SiH$_2$Cl$_2$ and NH$_3$).

3.2.5 Upper Cladding Layer Deposition:

As stated in the introduction section, the upper cladding layer affects the performance of the evanescent field sensing technique. This cladding layer is to be thick enough to protect the

core layer from environmental disturbance and at the same time thin enough to allow the mode

tail to interact with the analytes dispensed on top. In our first few samples we deposited a 20 nm

thin SiO_2 layer using PECVD system.

Table 3-4. Process recipe for SiO_2 deposition using PECVD system

Step: 1	
Pressure (mT)	700
ICP (W)	0
RIE (W)	0
Process Time (sec)	180
Temp (^{o}C)	360
Gases (sccm): N_2O 102, N_2 140, Ar/SiH_4: 12	
Step: 2	
Pressure (mT)	700
ICP (W)	400
RIE (W)	30
Process Time (sec)	Variable
Temp (^{o}C)	360
Gases (sccm): N_2O 102, N_2 140, Ar/SiH_4: 12	
Step: 3	
Pressure (mT)	250
ICP (W)	0
RIE (W)	0
Process Time (sec)	240
Temp (^{o}C)	360
Gases (sccm): N_2 250	

SiH_4 and N_2O gases were used for this purpose and a very slow deposition rate 350 Å/min was

obtained. Table:3-4 presents the active parameters in this PECVD process. The samples are then

cleaved with tweezer to obtain a nice, sharp facet suitable for light coupling. Some of the images

of the final device is presented in Fig. 3-7. In Figure 3-8, SEM images of the final device is presented. In some of our recently fabricated devices the upper cladding layer is switched to a thin TiO_2 layer using sputtering technique to match the surface chemistry of the biomaterials.

(a)	(b)	(c)
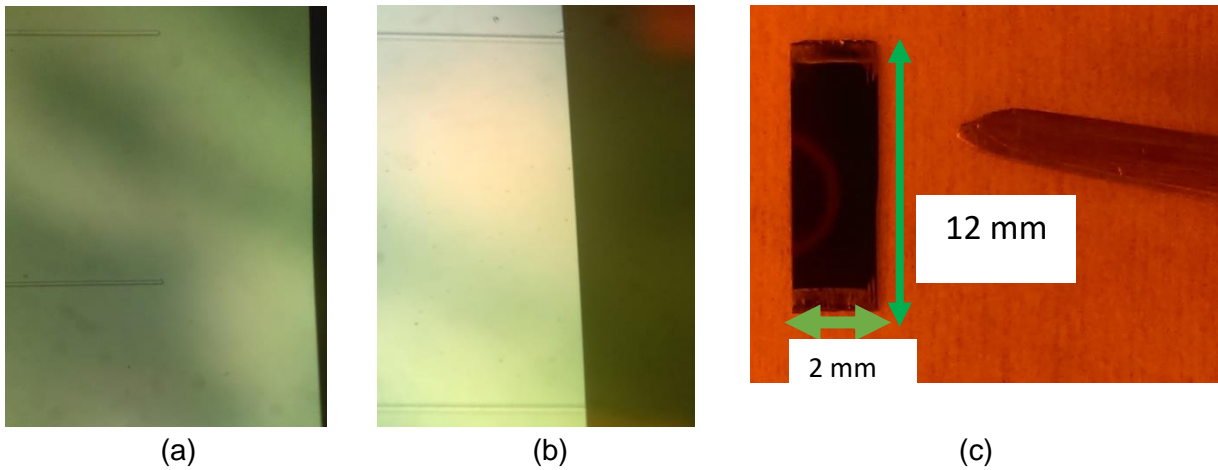
Fig. 3-7. (a) Waveguide facet before cleaving, (b) Waveguide facet after cleaving, (c) Final device dimensions compared to tweezer tip.
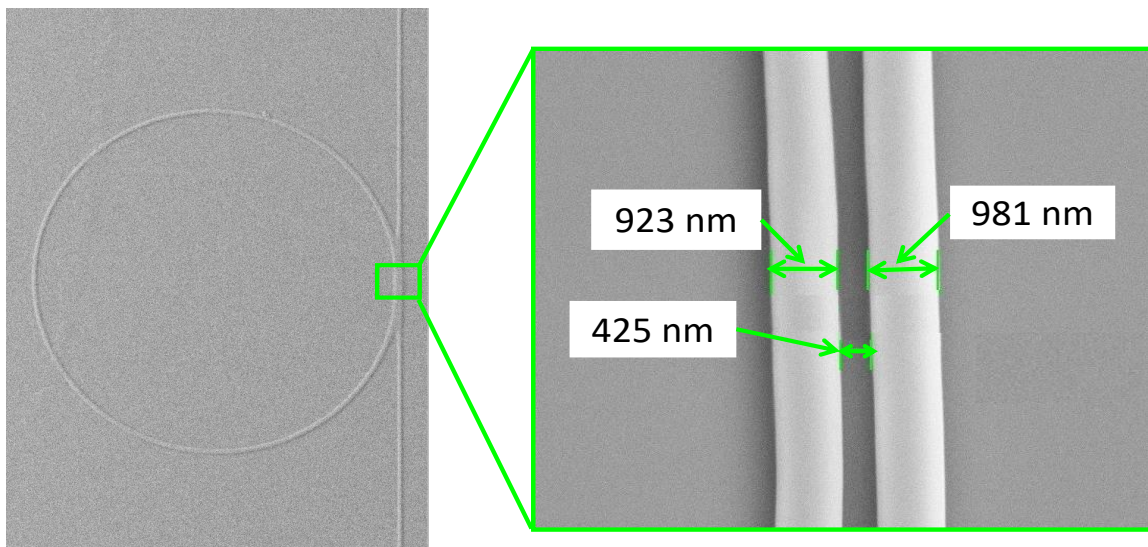
Fig. 3-8. Scanning electron microscope (SEM) image of the fabricated microring resonator. (Right) Detail view of the coupler area.

3.3 Characterization of Microring Resonator

With these SiO$_2$ coated samples we characterized the waveguide properties- propagation loss, FSR (Free Spectral Range) measurement and waveguide Q factor.

3.3.1 Experimental Setup:
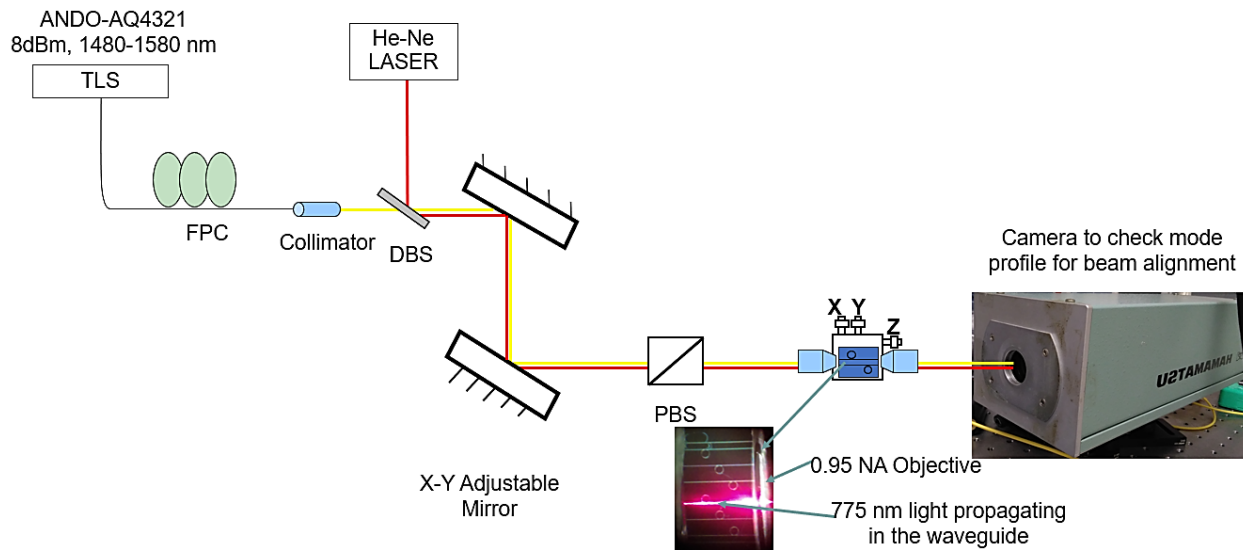
Fig. 3-9. Schematic of the free space set up for light coupling – red line resembles Visible light and Yellow line resembles IR light at 1550 nm

The experiment has been carried out in a free space coupling set up, as shown in Fig. 3-9, with Tunable Laser Source (TLS), ANDO- AQ 4321, as a source for 1550 nm light beam. This source has a bandwidth from 1480 nm- 1580 nm. The maximum power output from this source is 8 dBm. Alongside we use a He-Ne laser as a visible light source to check the light propagating through the waveguide. Both these sources are aligned collinearly by using a set of adjustable mirrors. The light beam from the TLS passes through a fiber polarization controller (FPC) and is collimated before passes through the Dichroic Beam Splitter(DBS) that passes both the visible and the 1550 nm light beam. The 1550 nm beam is transmitted while the visible light is reflected by the DBS.

A Polarization Beam Splitter (PBS) has also been inserted along the light path to pass only the TE (Vertical with respect to waveguide dimension) polarized light into the waveguide. The device is placed on an aluminum bar and positioned on a 3-axis piezoelectric controlled nano positioner stage. A microscope objective of 63x and 0.95 NA is placed to focus light from the free space onto the input facet of the waveguide. First, we use another microscope objective at the output of the bus waveguide to observe the mode profile of both the visible and IR light beam on a Hamamatsu camera as shown in Fig. 3-10.

(a)   (b)

Fig. 3-10. Mode profile of (a) Visible light beam and (b) IR light beam at 1550 nm

As both the light beam are co propagating we can focus the light beam, either the visible or IR, on the camera just by adjusting the Z axis position of the stage. After observing the single mode profile of the light beam as shown in Fig. 3-10, we switched the arrangement from Fig. 3-9 to Fig. 3-11 to obtain the transmission spectrum on an Optical Spectrum Analyzer (OSA). The output objective has been replaced by a Standard Single Mode Fiber (SSMF) to connect the OSA into the arrangement.
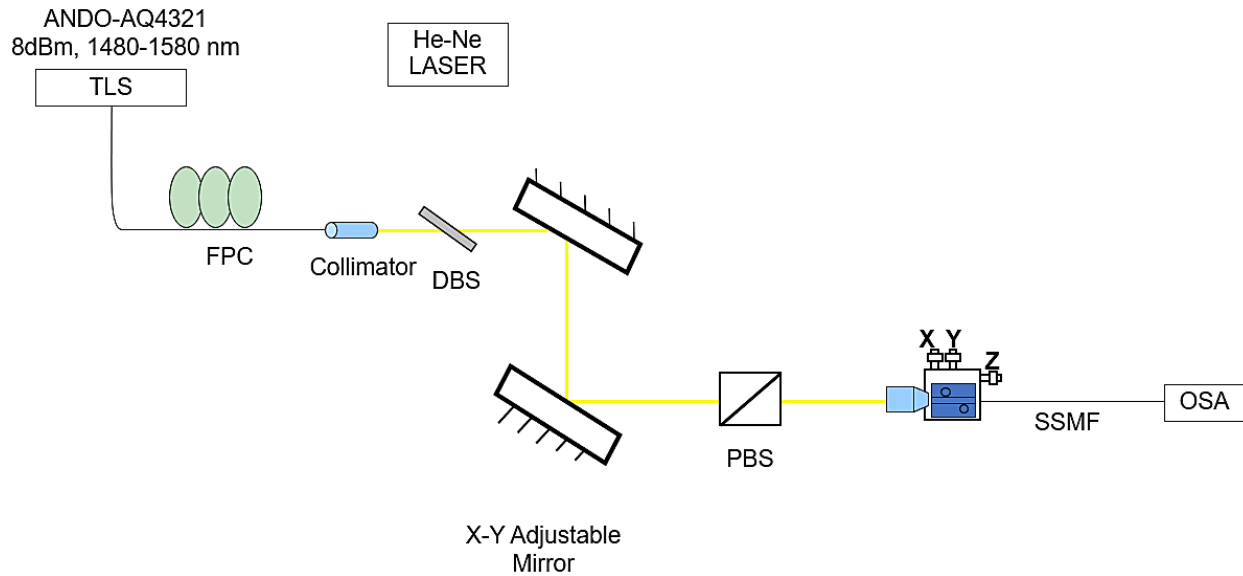
Fig. 3-11. Schematic of optical arrangement to observe transmission spectrum on OSA of incoming 1550 nm light beam passing through the fabricated waveguide

3.3.2 Waveguide Performance:

The width of the 1550 nm light beam has been characterized using knife edge method and the spot size was found to be well matched with the waveguide dimension.

Light Power Measurement:

After that the light power at different location along the free space path has been measured using optical power meter. It is found that the waveguide shows around 10-15 dB of total loss between the input and output facet as presented in Table 3-5.

Table 3-5. Optical Power measurement

Position of Power Meter Head	Optical Power (dBm)
Input Power	8 dBm
At the output of collimator	5.2 dBm
waveguide input facet (output of input objectives)	-13 dBm
Waveguide output facet using SSMF	-25 dBm

Free Spectral Range (FSR) and Quality Factor (Q):

The qualitative parameters of the fabricated waveguide are then evaluated from the transmission spectrum presented in Fig. 3-12. It shows FSR value of 1.38 nm, equivalent to 172 GHz. The quality factor, Q, of the resonance peak is also calculated as Q ≈ 5500 as presented in Fig. 3-13.

$$Q = \frac{\lambda_0}{\lambda_1 - \lambda_2} \tag{3.4}$$

where $\lambda_0 = 1543.569$ nm, $\lambda_1 = 1543.6993 nm\ and\ \lambda_2 = 1543.4192\ nm$
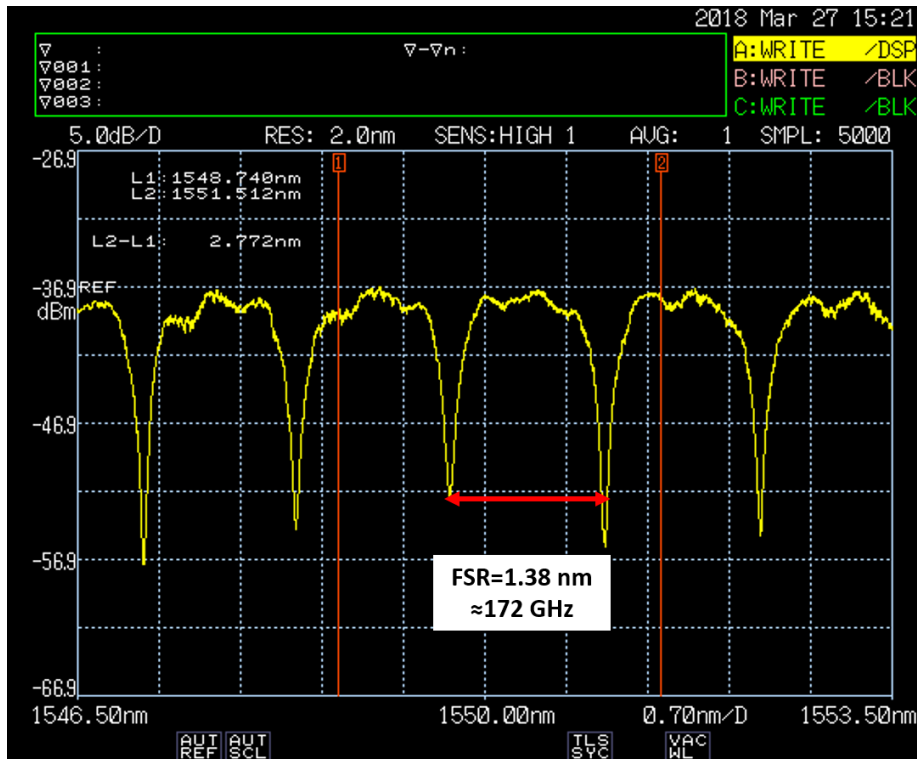
Fig. 3-12. Transmission spectrum of the IR light beam propagated through the ring resonator
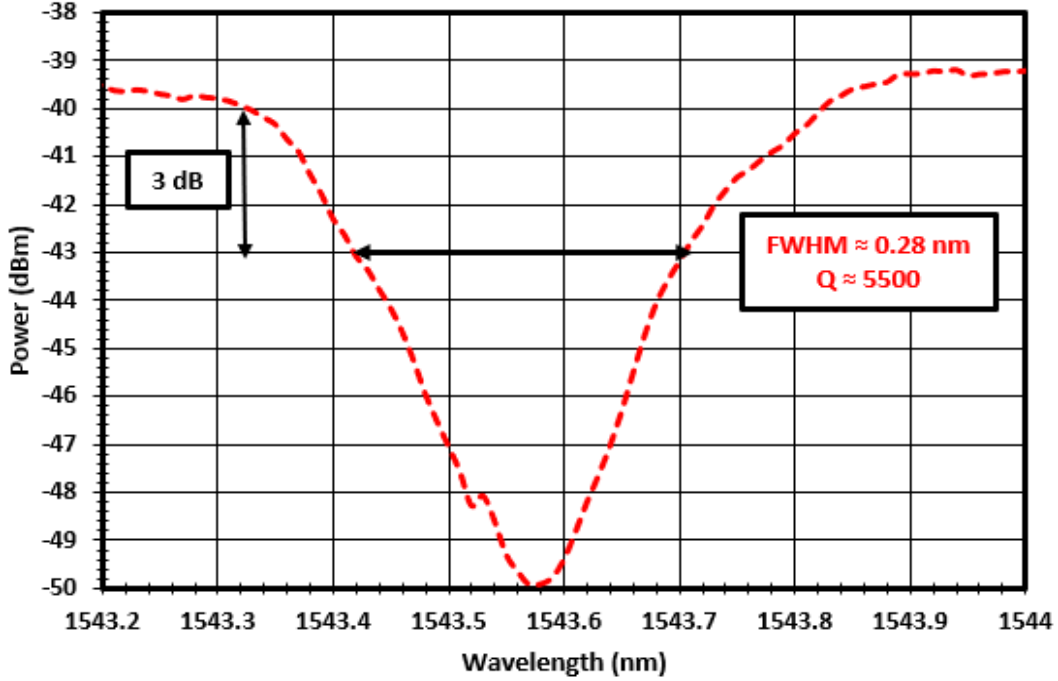
Fig. 3-13. Q factor measurement of the fabricated waveguide at a resonance at 1543.569 nm

3.3.3 Sensitivity Analysis of the Fabricated Microring Resonator:

The next important aspect of the device is the quantification of the sensing ability with respect to the variation in refractive index of the upper cladding. To evaluate this characteristic, we compared the transmission spectrum both in air (n=1) and DI water (n= 1.33) cladding as shown in Fig. 3-14.If the upper cladding material is changed the overall effective index of the waveguide structure will be changed. This variation in effective index, n_{eff} will be translated as a shift in the resonance condition stated in Equation (3-5). As a result, the resonance peaks will be shifted accordingly [72].

$$m\lambda = 2\pi n_{eff}R \tag{3-5}$$

Here, m= 1,2,3,…. , R= ring radius

Thus shift in resonance, $\quad\quad\quad\quad \Delta\lambda/\lambda = \Delta n_{eff}/n_{eff} \tag{3-6}$

For the case presented in Fig. 3-14, $\Delta\lambda = \lambda_2 - \lambda_1 = $ (1547.178-1546.647) nm= 0.531 nm.
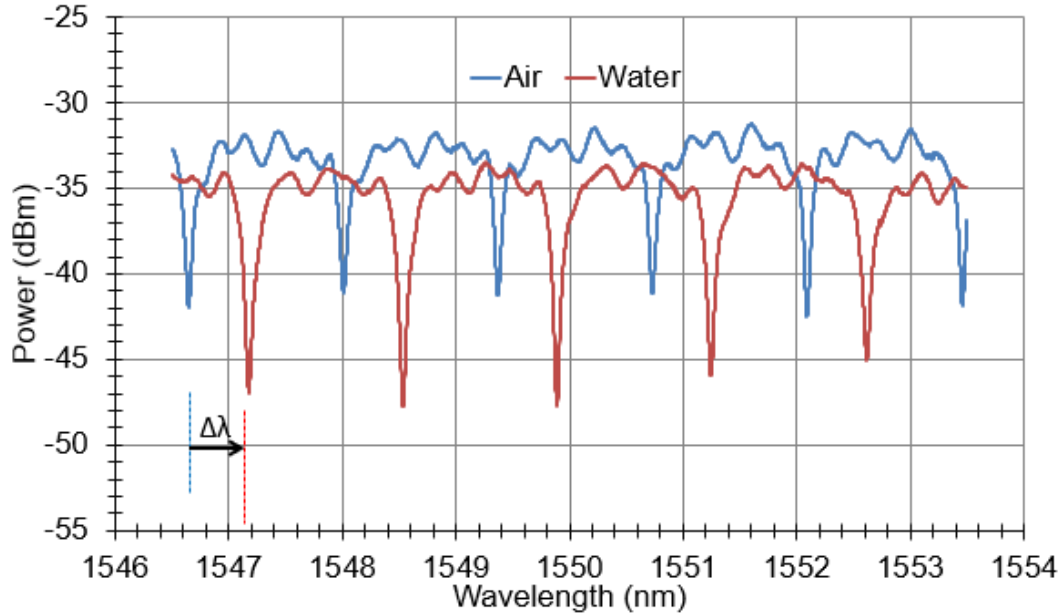
Fig. 3-14. Comparison of Transmission Spectrum with upper cladding as air (Blue Trace) and DI water (Maroon Trace).

In connection with Fig. 3-14, we conducted an experiment with DI water. The result of this experiment is included in one of our publications [26]. This publication focuses the performance of the fabricated microring resonator in aqueous environment. Here it has been shown that we can conservatively estimate its sensitivity by comparing the resonance frequencies with either air (*n*=1) or deionized (DI) water (*n*=1.33) as the top cladding layer. Figure 3-15 shows the transmitted spectrum for the microring resonator with air (red trace) and DI-water (green trace, region A) claddings. We observe free spectral range of 1.38 nm for DI-water cladding and a resonance shift of 0.47 nm between the air and DI-water cladding spectra. However, the 0.47-nm-shifted resonances do not belong to the same resonance order. To determine the number of free spectral ranges, by which the resonances of the same order are separated on these spectra, we have evaporated the DI water in the process of taking the green-trace spectrum in Fig. 3-15. The beginning of the spectrum (region A) corresponds to completely intact DI-water cladding, whereas the end of the spectrum (region C) corresponds to practically all DI water evaporated (the

resonances almost coincide with air-cladding resonances). The rate of OSA sweep has been chosen to be intentionally slow, so that the process of evaporation of the DI cladding is manifested in 18 resonances moving from right to left while the OSA is sweeping from left to right (region B in Fig. 3-15). This is expected, as the evaporation of the DI water reduces the effective waveguide index, shifting the resonances to higher frequencies (shorter wavelengths). The total resonance shift between the DI-water and air cladding cases can then be estimated as $17 \times (1.38$ nm FSR) $+ 0.47$ nm $= 23.93$ nm. Dividing this number by the 0.33 refractive index difference between the water and air, we obtain sensitivity estimate of 72.5 nm / RIU. This is a conservative estimate, based on large refractive index change from air to water, whereas the sensitivity to small index changes around the DI water index value is expected to be higher, owing to the longer reach of the mode tail into the water cladding, compared to the air.
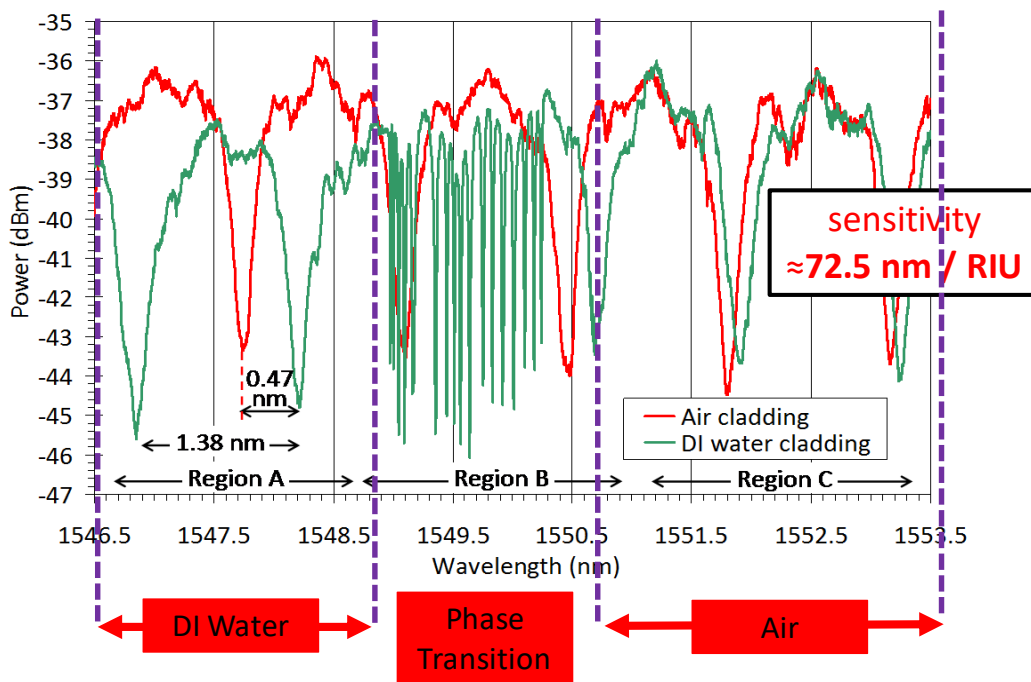
Fig. 3-15. Measurement of sensitivity of the sensor

3.4 Investigation of NPY Detection:

3.4.1 Sample Preparation and Functionalization of the Device Surface:

Here in this experiment with Neuropeptide Y (NPY) detection, we considered affinity-based immobilization methods such as protein G coupling [73]. The TiO_2-coated microring surface is functionalized with NPY attracting layer, represented by protein G, bound to the anti-NPY, and serving as NPY receptor [74]. The result presented in this section are a part of one of our conference publications [38]. The experimental steps are stated as follows:

1)   The microring resonator surface is first cleaned with acetone and methanol, followed by DI water rinse. Then 5 µL droplet of protein G (Abcam ab7458) of 50 µg/ml concentration is dispensed on the surface. With protein G added, the transmission spectrum is observed carefully and waited until the resonance peaks became sable- no more shift in wavelength. After over 30 minutes the device is rinsed with deionized (DI) water and with N_2 gas flow to remove any residue. Finally, DI water is added to obtain the steady state transmission spectrum for protein G. The spectrum is recorded, and DI water is blown away using N_2 gas flow.

2)   In next step anti-NPY (Abcam ab112473) with a concentration of 10 µg/ml has been dispensed on top of the device. In similar way, continuous transmission spectrum is obtained to locate the wavelength shift over a time span of more than 30 minutes. After rinsing with DI water and dried up, final steady state transmission spectrum with anti NPY attached is obtained with added DI water.

3)   In final step NPY (Abcam ab120208) solution at varied concentration is added on the device. The device already contains a layer of both protein G and Anti NPY. The transmission spectrum for NPY attachment is obtained and recorded. Finally, after more than 30 mins the device is rinsed in DI water and dried up with N_2 flow. The final steady state shift due to NPY

attachment is obtained in added DI water. All these biomaterials were dissolved in DI water and

5 µL of each solution were dispensed for the experiment.

3.4.2 Detection of NPY Concentration:

After all the tramission spectra are obtained, the final spectra in DI water for both Anti NPY and

NPY are compared to measure the shift in resonace due to NPY attachment as shown in Fig. 3-

16 for NPY concentration of 4 µg/ml where we see a resonance shift of 0.39 nm for over a time

period of 45 mins.
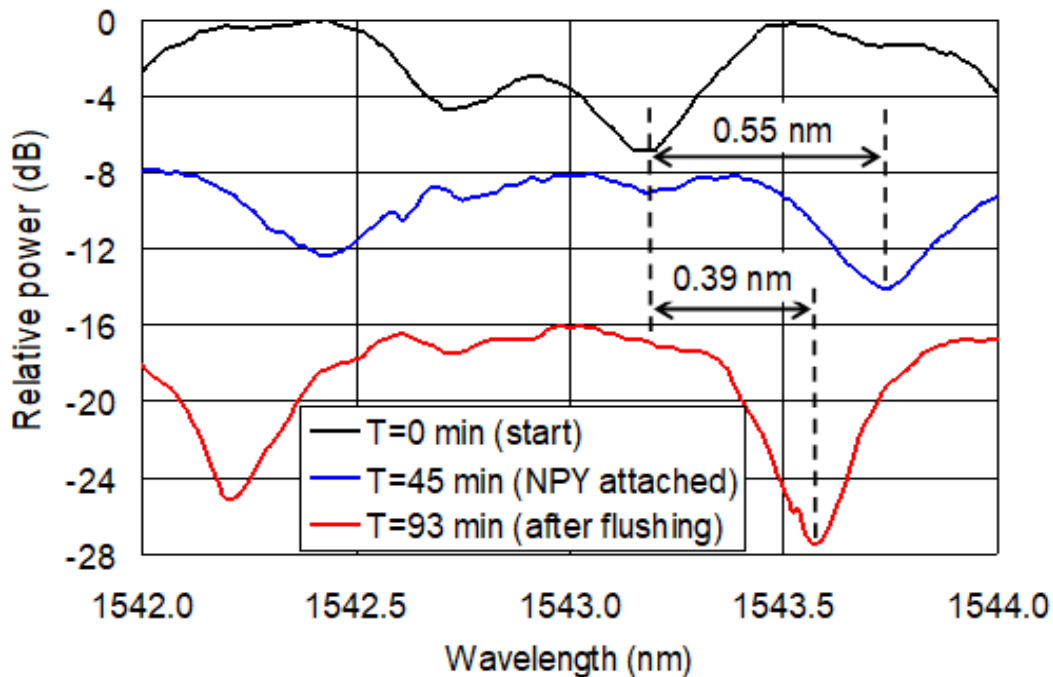
Fig. 3-16. Resonance shift due to NPY attachment over time [38].

Now tracking back a single resonance peak and plotting its location over time we can obtain the

Fig. 3-17 that shows the NPY association for 4 µg/ml of concentration. We see the resonance

shift due to NPY attachment reached its maximum value of 0.55 nm in 45 mins. After flushing the

device surface with DI water, the final steady state shift due to bounded NPY molecules is found

to be 0.39 nm. This same procedure has been carried out for other NPY concentration, i.e. 1 µg/ml, 2 µg/ml and 6 µg/ml as shown in Fig. 3-18.
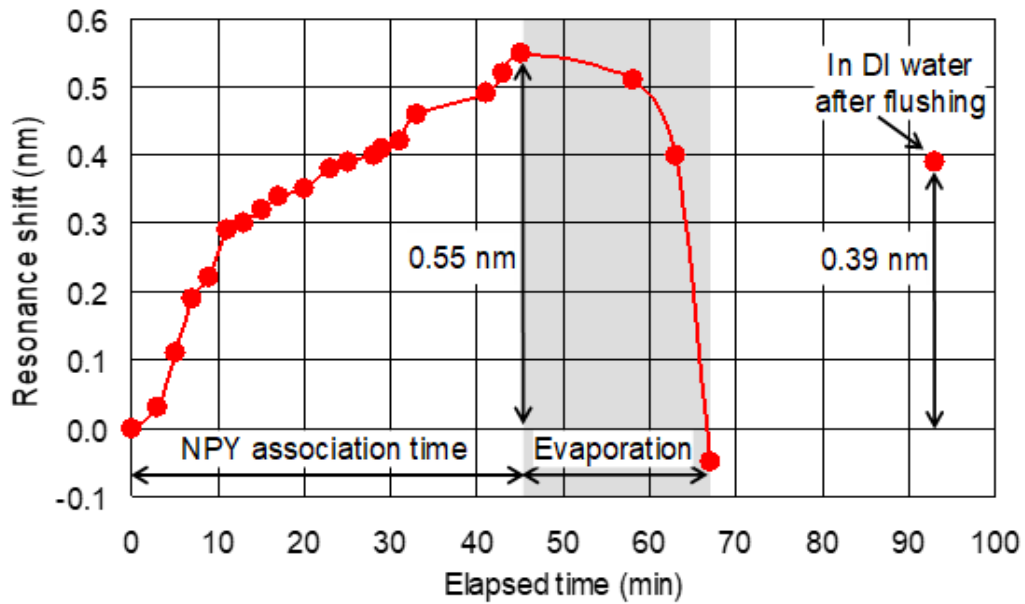
Fig. 3-17. NPY association curve for 4 µg/ml of concentration [38].
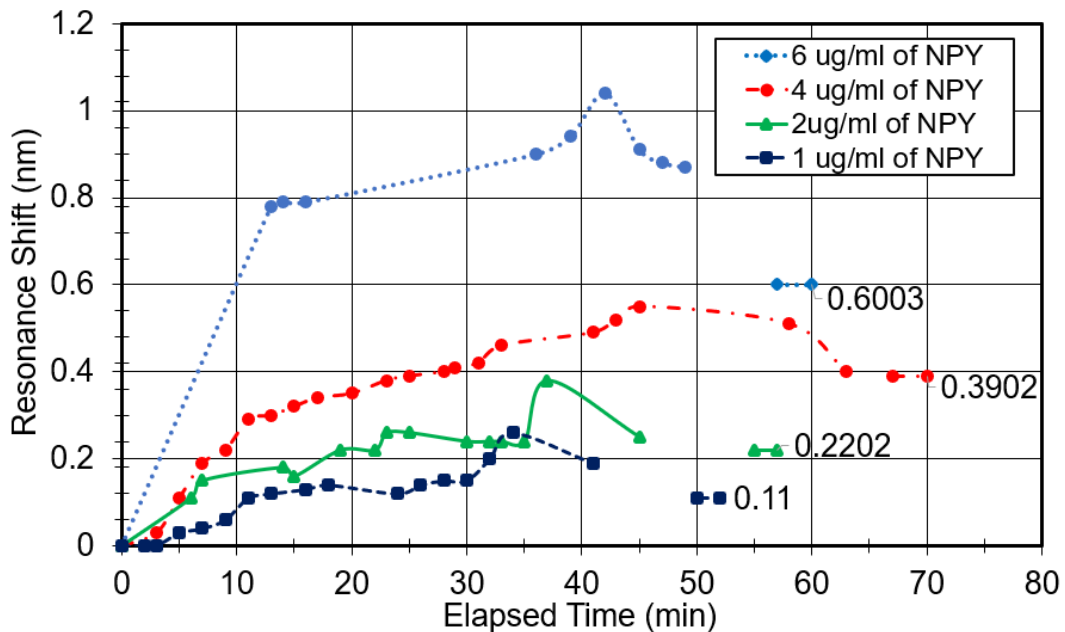
Fig. 3-18. Association curve for different concentration level of NPY

In Figure 3-19 the steady state values of resonance shift in DI water are plotted against each concentration of NPY, which conclusively states that the sensitivity of the fabricated sensor is about 0.1 nm/ (µg/ml).
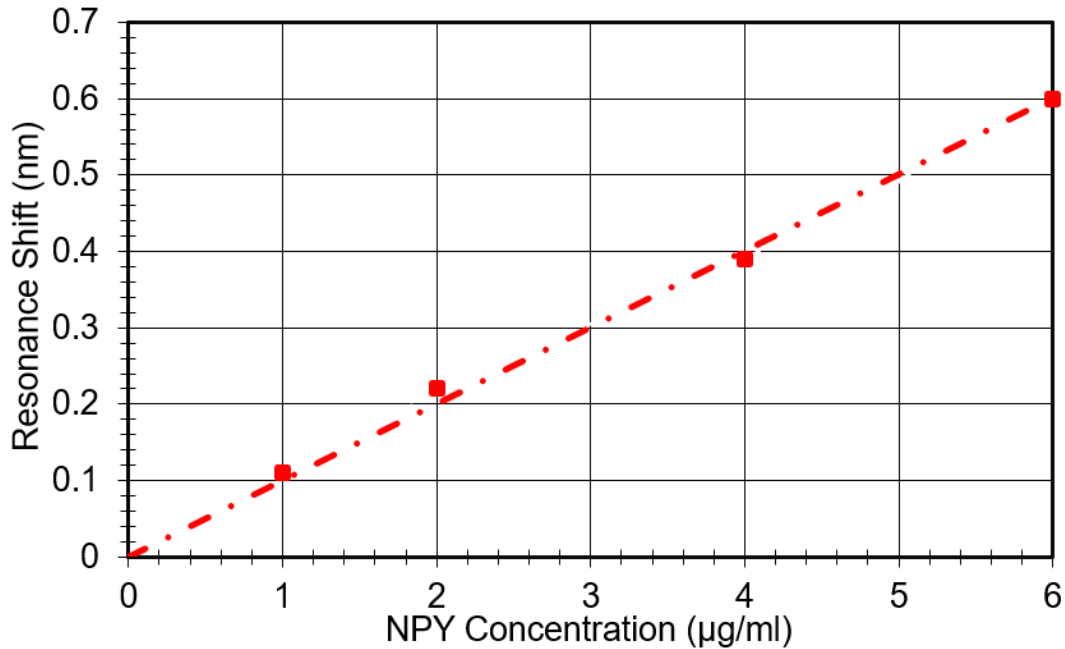
Fig. 3-19. Sensitivity analysis of the microring resonator with response to NPY detection

3.4.3 Experimental Limitations:

Some of the limitations observed in this experiment are:

1) **Detection limit up to 1 µg/ml-** NPY at concentration 0.5 µg/ml was unsuccessful.

2) **Room temperature effect-** the total procedure takes 6-8 hours of time duration. At some point the biomaterials got evaporated and left residue on the surface. Thus, experiment had to abandon. To overcome this problem, the ambient temperature was kept at 65° F (the lowest possible using room thermostat) in later experiments to reduce the evaporation rate of the solutions. So that the solutions do not dry up before steady state resonances

are obtained. The other way is to reduce to biomaterials' binding time by varying the concentration of surface functionalization layer.

3.5 Amplification of NPY Attachment Response

To address some of the limitations stated in previous section, the experimental procedure has been extended by including some extra steps as mentioned as sandwich assay [75]. These extra steps are mainly at the beginning and at the end of the procedure stated in section 3.3.1. Also, higher concentration of protein G at 100 µg/ml has been used to reduce the association time. Here two layers of anti NPY are used to sandwich the NPY. The first layer of anti NPY is called capture antibody and the later one is called indicator antibody [76].
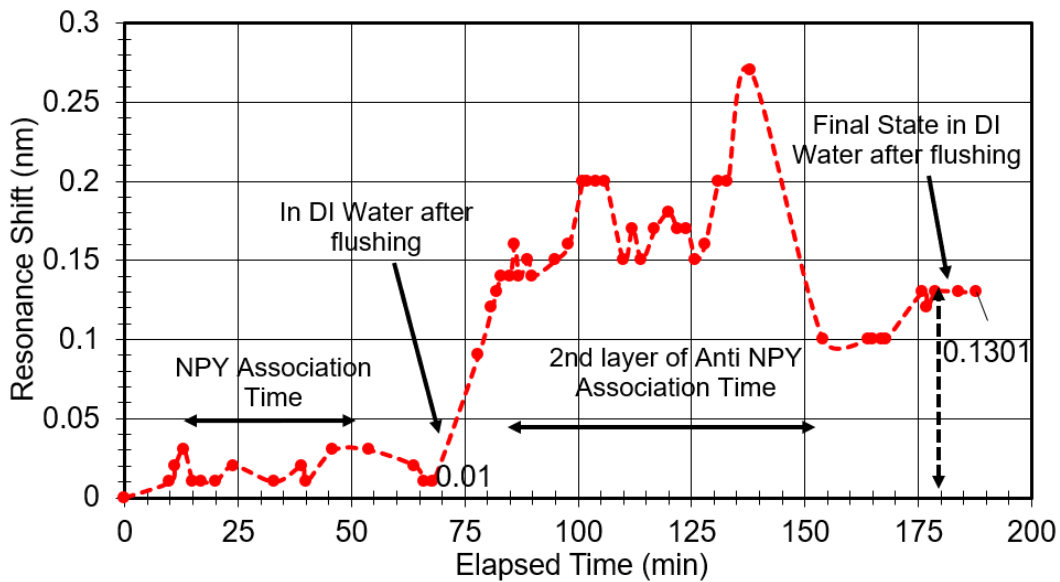
Fig. 3-20. Detection of NPY concentration of 0.25 µg/ml utilizing sandwiched assay technique

After cleaning the sensor surface with acetone and methanol, the device surface is inundated with 3% (3- Aminopropyl) triethoxysilane (APTES) in methanol solution to make the surface more hydrophilic [75]. Caution has been taken so that this solution does not touch the input facet of the waveguide. Solution droplets were dispensed carefully on the surface with a pipette. After about 30 mins, the device is rinsed with methanol and Di water. The three steps as stated in section

3.4.1 are then carried out. Finally, after obtaining the steady state shift due to NPY attachment

in DI water, second layer of anti NPY at 10 µg/ml concentration is dropped on the device surface

and the transmission spectra is recorded. After reaching the stable state of resonance shift, the

device is rinsed and final spectrum in DI water is obtained. At this time the target is to detect NPY

concentration lower than 1 µg/ml, so NPY at concentration 0.25, 0.5, 1 µg/ml has been used. The

sensor response with respect to 0.25 µg/ml of NPY concentration is plotted in Fig.3-20. Here, the

resonance shift for NPY association is almost negligible as in previous experiment with single

assay, but we observe a total shift of 0.1301 nm for 0.25 µg/ml NPY concentration when the

indicator anti NPY layer is added.
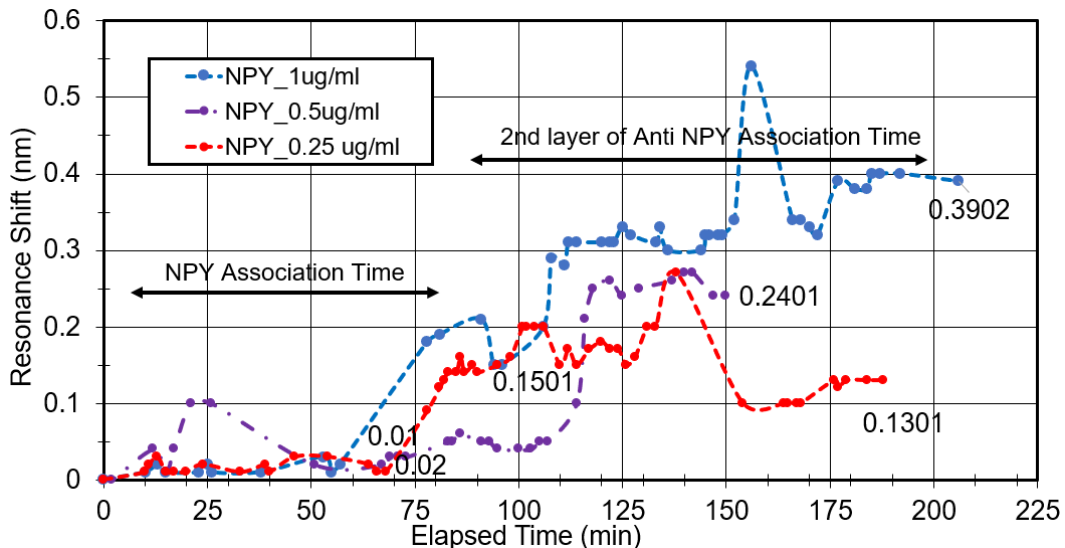
Fig. 3-21. Association curve for different NPY concentration in sandwiched assay technique.

We also carried out baseline correction, where all the procedural steps has been followed

with 0 µg/ml (simply DI water) NPY- DI water is added in between the two anti NPY layers as if it

is a solution of 0 µg/ml of NPY. In that case we saw a 0.06 nm of overall shift. This error can be

associated with day to day temperature variation and/or unsaturation of protein G layer by first

anti NPY layer. Taking this correction into account, we can state that in double assay technique

the 0.25 µg/ml of NPY created a 0.07 nm of resonance shift, whereas in previous experiment the

minimum detection limit was 1 µg/ml with 0.11 nm of resonance shift. We continued this experiment with other concentration of NPY- 0.5 and 1 µg/ml as shown in Fig. 3-21.

Table 3-6. Comparison between single sided anti NPY assay and double sided anti NPY assay

NPY Concentration (µg/ml)	Resonance shift after NPY Association in single assay (nm)	Resonance shift after NPY Association In double assay (nm)	Total Resonance shift with indicator anti NPY attachment in double assay (nm)
0.25	N/A	0.01	0.07
0.5	0	0.02	0.18
1	0.11	0.15	0.33

The steady state value of resonance shift in DI water after the NPY association and after the indicator anti NPY layer for the double sided anti NPY assay are tabulated in Table 3-1. Table 3-1 also included the result from our previous experiment of single sided anti NPY assay. Comparing the results, we can conservatively ascertain that this sandwich assay technique amplified the signal almost by 3 times as shown in Fig. 3-22.
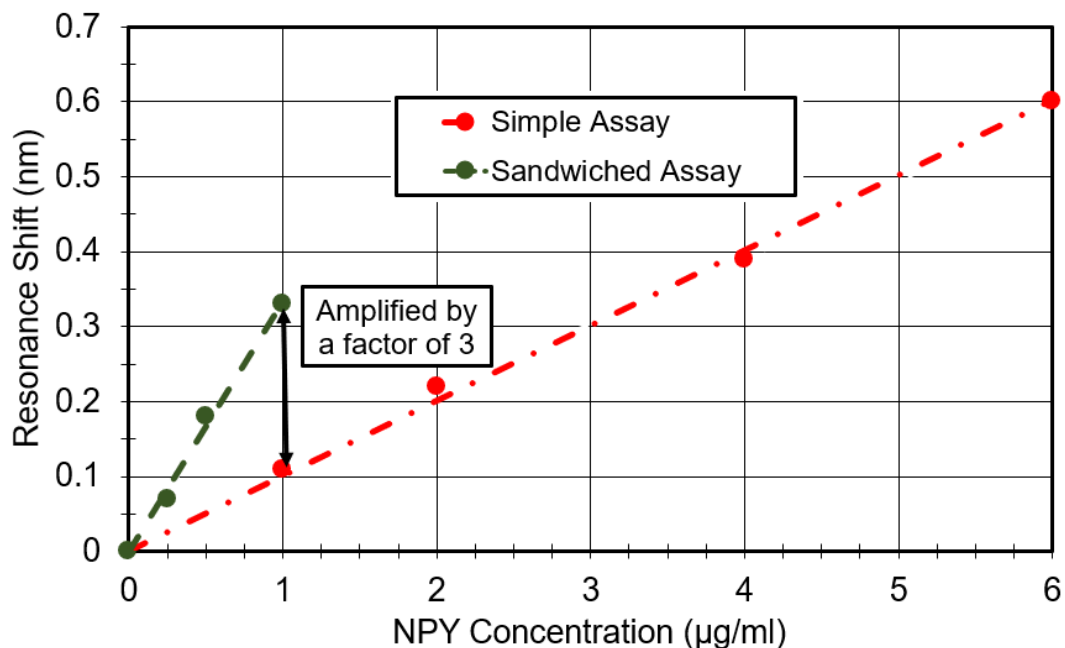
Fig. 3-22. Comparison between simple assay and sandwiched assay technique

3.6 Summary:

To summarize, we have designed, fabricated, and functionalized a silicon-nitride microring resonator for detection of Neuropeptide Y (NPY) in aqueous environment. The device shows a sensitivity of ~0.11 nm/ (μg/ml) concentration of NPY in single-sided anti-NPY assay. This experiment indicates that the concentrations down to ~1 μg/ml should be easily measurable. It is also shown that the detection limit can be extended into sub μg/ml concentration of NPY by utilizing double-sided anti-NPY assay.   Using this sandwiched technique, the sensitivity is increased by three times- ~ 0.33 nm/ (μg/ml) concentration of NPY.

Chapter 4

Conclusions

The vision of this thesis work was to establish Silicon Nitride as a promising material for both linear and nonlinear optics applications. As an exemplary application in nonlinear optics, SiN waveguide with polymer cladding layer has been designed and optimized to generate second harmonic of a 1550-nm wave. We have shown that phase matching condition between the participating waves- 0th-order mode of 1550 nm fundamental wave and 2nd-order mode of 775 nm wave is achievable in a simple single channel waveguide, but the effective nonlinearity is very low due to a poor nonlinear overlap integral. On the other hand, a slot waveguide with optimized dimensions (589 nm x 450 nm x 200 nm) and nonlinear polymer filling either the slot or both the slot and upper cladding has an order-of-magnitude higher nonlinear overlap integral, $A_{eff} \sim 16$ μm^2. We have also shown that both the conditions of phase matching and nonlinear overlap integral are robust to fabrication tolerance for a waveguide bending with radii as small as $\sim$150 μm, This result is definitely promising for the development of waveguide- and microresonator-based nonlinear photonic integrated circuits.

We also demonstrated the applicability of SiN microring resonator within the regime of linear optics by fabricating and characterizing a refractive index sensor. The fabrication is carried out by CMOS processes: LPCVD, E-beam lithography, DRIE, Annealing and PECVD. The microring

resonator shows a Q factor of 5500, which is quite reasonable for a thin upper cladding layer of 20 nm. The sensor surface is functionalized with protein G to utilize affinity based immobilized detection technique for neuropeptide Y (NPY), a 36 amino-acid neuropeptide involved in several physiochemical activities in human body. The experiment has been carried out in free space coupling setup with tunable laser source at 1550 nm. The attachment of the NPY on the device surface has been confirmed by observing shift in resonance peaks of the transmission spectrum on optical spectrum analyzer (OSA). We then relate this shift in resonance to the concentration of NPY and found a sensitivity of 0.1 nm/(μg/ml). The sensitivity is further amplified by a factor of 3 when we use sandwich assay, and NPY concentration down to 0.25 μg/ml is easily detected, with the detection limit imposed mainly by the OSA.

In conclusion, we have demonstrated great potential of silicon nitride as a common platform for optical device integration for both nonlinear-optics (e.g.,SHG) and linear-optics (e.g., NPY sensing) applications. This research work will hopefully help future researchers to explore more intriguing devices on silicon nitride platform.

Appendix I

List of Publications

Project I:

Investigation of Hybrid Silicon-Nitride/Polymer Waveguides for Second-Harmonic Generation

[1] S. Das et al, "Hybrid silicon-nitride / polymer waveguide for nonlinear-optics applications," *CLEO conference*, San Jose, CA, May 13–18, 2018, paper JTu2A.77.

[2] S. Das et al, "Robustness of second-harmonic generation in a hybrid SiN / polymer waveguide," *IEEE Photonics Society's Research and Applications of Photonics in Defense (RAPID) Conference*, Miramar Beach, FL, August 22–24, 2018, paper ThC2.7.

[3] S. Das et al, "Investigation of Hybrid Silicon-Nitride/ Polymer Waveguides for Second-Harmonic Generation", IEEE Photon. J. 11 (2019).

Project II:

Investigation of Neuropeptide Y Detection by a Silicon- Nitride Microring Resonator

[1] S. Das et al, "Investigation of Si3N4 microring resonator for bio-chemical sensing applications," *Frontiers in Optics 2018*, paper JW3A.98.

[2] S. Das et al, "Investigation of Neuropeptide Y Detection by a Silicon-Nitride Microring Resonator", *IEEE Photonics Society's Research and Applications of Photonics in Defense (RAPID) Conference*, Miramar Beach, FL, August 19–21, 2019, paper WC1.4.

[3] (Invited) "Optical biosensing with silicon-nitride microresonators," S. Das, S. C. Samudrala, K. J. Lee, R. Magnusson, B. R. Wenner, J. W. Allen, M. S. Allen, and **M. Vasilyev**, *the IEEE Photonics Society's Research and Applications of Photonics in Defense Conference (RAPID) conference*, Miramar Beach, FL, August 19–21, 2019, paper TuC1.1

Bibliography

[1] W. Bogaerts and L. Chrostowski, "Silicon Photonics Circuit Design: Methods, Tools and Challenges", Laser Photonics Rev. ,12, 1700237, 2018.

[2] J. Leuthold et al, "Nonlinear silicon photonics", Nature Photon. 4, 535-544, 2010

[3] J. B. Lasky, "Wafer bonding for silicon-on-insulator technologies", Appl. Phys. Lett. 48 (1), 1986.

[4] R. baets, "Silicon Photonics: silicon nitride versus silicon-on-insulator", OFC conference 2016, paper Th3J.1.

[5] B. J. Eggleton et al, "Chalcogenide photonics," Nature Photon. 5, 141–148 (2011).

[6] D. J. Moss et al, "New CMOS-compatible platforms based on silicon nitride and Hydex for nonlinear optics," Nature Photon. 7, 597–607 (2013).

[7] F. Da Ros et al, "Characterization and optimization of a high-efficiency AlGaAs-on-Insulator-based wavelength converter for 64-and 256-QAM signals," J. Lightwave Technol. 35, 3750–3757 (2017).

[8] Z. Tong et al, "Noise performance of a frequency non-degenerate phase-sensitive amplifier with un-equalized inputs," Opt. Lett. 36, 722–724 (2011).

[9] Z. Tong et al, "Modeling and measurement of the noise figure of a cascaded non-degenerate phase-sensitive parametric amplifier," Opt. Express 18, 14820–14835 (2010).

[10]   F. Flamini et al, "Photonic quantum information processing: a review," Rep. Prog. Phys. 82, 016001 (2019).

[11] J. Leuthold et al, "Silicon organic hybrid technology – a platform for practical nonlinear optics," Proc. IEEE 97, 1304–1316, 2009.

[12] L. Alloatti et al, "Second-order nonlinear silicon-organic hybrid waveguides," Opt. Express 20, 20506–20515, 2012.

[13] J. X.J.Zhang and K. Hoshino, " Molecular Sensors and Nanodevices-Principles, Designs and Applications in Biomedical Engineering" Chapter 2, 43-101, Elsevier Publication, ISBN: 978-1-4557-7631-3, 2014.

[14] C. H. Henry *et al*, "Low loss SiN-SiO$_2$ optical waveguides on Si," Appl. Opt. **26**, 2621–2624 (1987).

[15] W. Stutius and W. Streifer, "Silicon nitride films on silicon for optical waveguides," Appl. Opt. **16**, 3218–3222 (1977).

[16] L. Yi *et al*, "Characterization of hybrid InP-TriPleX photonic integrated tunable lasers based on silicon nitride (Si$_3$N$_4$/SiO$_2$) microring resonators for optical coherent system", IEEE Photon. J. **10**, 1400108 (2018).

[17] C. J. Cullen *et al*, "Thin-film silicon nitride on electro-optic materials for a novel modulator architecture,"

IEEE Research and Applications of Photonics In Defense (RAPID) conference, Miramar Beach, FL, August 22–24, 2018, paper ThC2.6.

[18] K. Ikeda et al., "Thermal and Kerr nonlinear properties of plasma-deposited silicon nitride/ silicon dioxide waveguides,"258 Opt. Exp., vol. 16, pp. 12987–12994, 2008.

[19] A. R. Johnson et al., "Octave-spanning coherent supercontinuum generation in a silicon nitride waveguide," Opt. Lett.,260 vol. 40, pp. 5117–5120, 2015.

[20] K. J. A. Ooi et al., "Pushing the limits of CMOS optical parametric amplifiers with USRN: Si_7N_3 above the two-photon262 absorption edge," Nature Commun., vol. 8, 2017, Art. no. 13878.

[21] H. Guo et al., "Mid-infrared frequency comb via coherent dispersive wave generation in silicon nitride nanophotonic waveguides," Nature Photon., vol. 12, pp. 330–335, 2018.

[22] H. Zhao et al., "Stimulated Raman spectroscopy of analytes evanescently probed by a silicon nitride photonic integrated waveguide," Opt. Lett., vol. 43, pp. 1403–1406, 2018.

[23] M. Yang et al., "An octave-spanning optical parametric amplifier based on a low dispersion silicon rich nitride waveguide," IEEE J. Sel. Topics Quantum Electron., vol. 24, no. 6, Nov./Dec. 2018 Art. No. 8300607.

[24] C. A. Barrios et al, "Slot-waveguide biochemical sensor," Opt. Lett. 32, 3080–3082 (2007).

[25] P. Kaur and M. R. Shenoy, "Highly sensitive refractive index sensor based on silicon nitride strip waveguide directional coupler," IEEE Sensors Lett. 2, 3500504 (2018).

[26] S. Das et al, "Investigation of Si_3N_4 microring resonator for bio-chemical sensing applications," Frontiers in Optics 2018, paper JW3A.98.

[27] J. L. Arlett et al, "Comparative advantages of mechanical biosensors." *Nature nanotechnology* 6, no. 4, 203-215 (2011).

[28] P. Mehrotra *et al.*, "EM-Wave Biosensors: A Review of RF, Microwave, mm-Wave and Optical Sensing", Sensors, **19**,1013 (2019).

[29] Y. Sun and X. Fan, "Optical ring resonators for biochemical and chemical sensing," Anal. Bioanal. Chem. 399, 205–211 (2011).

[30] R. W. Boyd, "Nonlinear Optics", 3rd Edition, Academic Press, 2008

[31] M. Cazzanelli et al, "Second-harmonic generation in silicon waveguides strained by silicon nitride", Nature Mat. 11, 148–154 (2012).

[32] J. S. Levy et al, "Harmonic generation in silicon nitride ring resonators", Opt. Express 19, 11415–11421 (2011).

[33] R. E. P. de Oliveira and C. J. S. de Matos, "Quasi-phase-matched second harmonic generation in silicon nitride ring resonators controlled by static electric field," Opt. Express 21, 32690–32698 (2013).

[34] A. Farsi et al, "Large Effective $\chi(2)$ Nonlinearity via Coherent Photon Conversion on a Si_3N_4 Chip," CLEO conference, San Jose, CA, May 14–19, 2017, paper FTu3D.5.

[35] S. Das et al, "Hybrid silicon-nitride / polymer waveguide for nonlinear-pptics applications," CLEO conference, San Jose, CA, May 13–18, 2018, paper JTu2A.77.

[36] S. Das et al,"Robustness of second-harmonic generation in a hybrid SiN / polymer waveguide,"IEEE Photonics Society's Research and Applications of Photonics in Defense Conference (RAPID) conference, Miramar Beach, FL, August 22–24, 2018, paper ThC2.7.

[37] S. Das et al," Investigation of Hybrid Silicon-Nitride/ Polymer Waveguides for Second-Harmonic Generation", IEEE Photon. J. 11 (2019).

[38] S. Das et al, "Investigation of Neuropeptide Y Detection by a Silicon-Nitride Microring Resonator", IEEE Photonics Society's Research and Applications of Photonics in Defense Conference (RAPID) 2019.

[39] Y. B. Kwon and M. Vasilyev, "Mode-selective frequency up-conversion in a $\chi(2)$ waveguide," Proc. SPIE 8964, 8964-21 (2014).

[40] S. V. Rao et al, "Nonlinear frequency conversion in semiconductor optical waveguides using birefringent, modal and quasi-phase-matching techniques," J. Opt. A: Pure and Appl. Opt. 6, 569–584 (2004).

[41] M. Annamalai et al, "Phase-sensitive multimode parametric amplification in parabolic-index waveguide," IEEE Photon. Technol. Lett. 24, 1949 (2012).

[42] M. Annamalai et al, "Spatial modes of phase-sensitive parametric image amplifiers with circular and elliptical Gaussian pumps," Opt. Express 19, 26710–26724 (2011).

[43] M. Annamalai et al, "Compact representation of the spatial modes of a phase-sensitive image amplifier," Opt. Express 21, 28134–28153 (2013).

[44] M. Vasilyev and Y. B. Kwon, "Spatial-mode-selective quantum frequency conversion in nonlinear waveguides," Proc. SPIE 9505, 95050O (2015).

[45] Y. B. Kwon et al, "Experimental demonstration of spatial-mode-selective frequency up-conversion in a multimode $\chi(2)$ waveguide," CLEO conference, San Jose, CA, June 5–10, 2016, paper STh3P.4.

[46] Y. B. Kwon et al, "Single-photon-level spatial-mode-selective frequency up-conversion in a multimode $\chi^{(2)}$ waveguide," CLEO conference, San Jose, CA, May 14–19, 2017, paper FF2E.1.

[47] BeamPROP software manual, RSoft / Synopsys, https://www.synopsys.com/optical-solutions/rsoft/passive-device-beamprop.html .

[48] T. Bååk, "Silicon oxynitride; a material for GRIN optics," Appl. Opt. 21, 1069–1072 (1982).

[49] J. M. Chavez Boggio et al, "Dispersion engineered silicon nitride waveguides by geometrical and refractive-index optimization," J. Opt. Soc. Am. B 31, 2846–2857 (2014).

[50] Q. Xu et al, "Experimental demonstration of guiding and confining light in nanometer-size low-refractive-index material," Opt. Lett. 29, 1626 (2004).

[51] M. Fujii, J. Leuthold, and W. Freude, "Dispersion relation and loss of subwavelength confined mode of metal-dielectric-gap optical waveguides," IEEE Photon. Technol. Lett. 21, 362–364 (2009).

[52] L. Zhang et al, "Flattened dispersion in silicon slot waveguides," Opt. Express 18, 20529–20534 (2010).

[53] V. R. Almeida et al, "Guiding and confining light in void nanostructure," Opt. Lett. 29, 1209–1211 (2004).

[54] H. Tian et al, "Dynamics of nanoparticles trapped on an Integrated slot waveguide with a high index contrast," OSA Optics in Life Sciences Congress, San Diego, CA, April 2–5, 2017, paper OtS1D.4.

[55] S. Kim and M. Qi, "Broadband second-harmonic phase-matching in dispersion engineered slot waveguides," Opt. Express 24, 773–786 (2016).

[56] C. Koos et al, "Nonlinear high index-contrast waveguides with optimum geometry," Bragg Gratings, Photosensitivity and Poling in Glass Waveguides (BGPP) and Nonlinear Photonics (NP) OSA Topical Meeting, Quebec City, Canada, September 2–6, 2007, paper JWA2.

[57] A. Gondarenko, J. S. Levy, and M. Lipson, "High confinement micron-scale silicon nitride high Q ring resonator," Opt. Express 17, 11366 (2009).

[58] J. Luo et al, "Efficient wafer-scale poling of electro-optic polymer thin films on soda-lime glass substrates: large second-order nonlinear coefficients and exceptional homogeneity of optical birefringence," Opt. Mater. Express 7, 1909–1916 (2017).

[59] P. A. Anderson, B. S. Schmidt, and M. Lipson, "High confinement in silicon slot waveguides with sharp bends," Opt. Express 14, 9197–9202 (2006).

[60] Datasheet- Neuropeptide Y (NPY) (human, rat), Endogenous neuropeptide (ab120208), https://www.abcam.com/neuropeptide-y-npy-human-rat-ab120208.html .

[61] S. C. Samudrala, "Silicon Nitride Devices for Nonlinear and Quantum Optics Applications", PhD Dissertation, University of Texas at Arlington, 2016.

[62] TYSTAR LPCVD Processes, https://en.tystar.com/technology/lpcvd-process.

[63] Datasheet, Negative tone photoresist series ma-N2400,

https://www.microresist.de/en/products/negative-photoresists/e-beam-deep-uv-lithography/ma-n-2400-mr-ebl-6000-series

[64] J.C. Nabity, "User's manual for NPGS v9", Lithography Systems, 2009.

[65] "Ebeam/FIB 1540XB Crossbeam Standard Operating Procedure V1", Zeiss 1540XB Cross Beam FIB FE SEM,2014.

[66] "Reactive Ion Etching", https://www.corial.com/en/technologies/reactive-ion-etching-rie/

[67] DRIE User Guide, Shimadzu Institute Nanotechnology Research Center, UTA.

[68] B.D. pant and U. S. Tandon, "Etching of Silicon Nitride in CCl_2F_2, CHF_3, SiF_4 and SF_6 Reactive Plasma: A Comparative Study, Plasma Chem. And Plasma Proc. **19**, 4, 1999.

[69] Application Note, "Plasma Etching of Silicon Nitride and Silicon Dioxide", Plasma Therm I.P., 1992.

[70] Doris K. T. Ng *et al.* "Exploring High Refractive Index Silicon-Rich Nitride Films by Low Temperature Inductively Coupled Plasma Chemical Vapor Deposition and Applications for Integrated Waveguides", ACS Appl. Mater. Interfaces, Vol 7, pp 21884- 21889, 2015.

[71] R. Moreira, S. Gundavarapu and D. J. Blumenthal, "Programmable eye-opener lattice filter for multi-channel dispersion compensation using an integrated compact low-loss silicon nitride platform", *Optics Express*, Vol. 24, No. 15, pp 16732- 16742.

[72] W. Bogaerts et al, "Silicon microring resonators," Laser Photon. Rev. 6, 47–73 (2012).

[73] K. J. Lee, R. Magnusson, B. R. Wenner, J. W. Allen, and M. S. Allen, "Guided-Mode Resonance Biosensors: Quantifying the Binding of Neuropeptide Y to its Antibody," Frontiers in Optics 2017, paper JTu2A.60.

 [74] R. Magnusson et al, "The guided-mode resonance biosensor: principles, technology, and implementation," Proc. SPIE 10510, 105100G (2018).

[75] R. Magnusson et al, "Guide-mode resonance sensing of neuropeptide-Y with a sandwich assay achieving pg/mL detection", Proc. of SPIE, **11020,** 2019.

[76] E. Grouzmann et al, "A Sensitive and Specific Two-Site, Sandwich- Amplified Enzyme Immunoassay for Neuropeptide", Peptides,**13**, 1049-1054, 1992.

Biography

Subrata Das received his B.Sc and M.Sc degree in Applied Physics, Electronics and Communication Engineering (APECE) from the University of Dhaka, Bangladesh in 2007 and 2008 respectively. He obtained a second master's degree in Photonics under the Erasmus Mundus MSc. in Photonics (EMMP) program coordinated by the University of Ghent, Belgium. He spent the first year of study at the Royal Institute of Technology (KTH), Sweden and second year of study at the Free University of Brussels (VUB), Belgium. He joined as a Lecturer at the Dept. of APECE, University of Dhaka in 2010 and taught courses on Optics and Circuit Analysis until 2014. In Fall 2014, he started his PhD program at the department of Electrical Engineering, University of Texas at Arlington under the supervision of Professor Michael Vasilyev. His PhD research is focused on the SiN platform for both linear and nonlinear optics applications. During this program he published several peer reviewed articles and attended top notched conferences (CLEO, FIO, RAPID) in the field of photonics. He also obtained travel grants to attend these conferences. He worked as a Graduate Teaching Assistant (GTA) for several graduate and undergraduate level courses in the Dept. of Electrical Engineering, UTA. For his dedicated performance he received Outstanding GTA Award in Spring 2018 semester and was selected as the Student Employee of the Year (2018-2019). He received his PhD from University of Texas at Arlington in 2019.